MODELING OF FLEXIBLE NEEDLE INSERTION IN MOVING TISSUE

A THESIS
SUBMITTED TO THE DEPARTMENT OF COMPUTER ENGINEERING
AND THE GRADUATE SCHOOL OF ENGINEERING AND SCIENCE
OF BILKENT UNIVERSITY
IN PARTIAL FULFILLMENT OF THE REQUIREMENTS
FOR THE DEGREE OF
MASTER OF SCIENCE

By
Aslı Deniz Güven
August, 2012

I certify that I have read this thesis and that in my opinion it is fully adequate, in scope and in quality, as a thesis for the degree of Master of Science.

Asst. Prof. Dr. Selim Aksoy (Supervisor)

I certify that I have read this thesis and that in my opinion it is fully adequate, in scope and in quality, as a thesis for the degree of Master of Science.

Asst. Prof. Dr. Uluç Saranlı (Co-Supervisor)

I certify that I have read this thesis and that in my opinion it is fully adequate, in scope and in quality, as a thesis for the degree of Master of Science.

Assoc. Prof. Dr. Cenk Çavuşoğlu

I certify that I have read this thesis and that in my opinion it is fully adequate, in scope and in quality, as a thesis for the degree of Master of Science.

Asst. Prof. Dr. Çiğdem Gündüz Demir

Approved for the Graduate School of Engineering and Science:

Prof. Dr. Levent Onural
Director of the Graduate School

ABSTRACT

MODELING OF FLEXIBLE NEEDLE INSERTION IN MOVING TISSUE

Aslı Deniz Güven
M.S. in Computer Engineering
Supervisors: Asst. Prof. Dr. Selim Aksoy and Asst. Prof. Dr. Uluç Saranlı
August, 2012

Steerable needles can be used for minimally invasive surgeries to reach clinical targets which were previously inaccessible by rigid needles. Using such flexible needles to plan an insertion for these procedures is difficult because of the nonholonomic motion of the bevel-tip needles and the presence of anatomical obstacles. In this work, we take into consideration another property of such procedures being the tissue motion as well as these. For instance in a minimally invasive cardiac surgery one should take into account the effect of the heart's beating motion on the needle during its insertion or in any other procedure the effect of human breathing. In this thesis, we develop a motion model for a bevel-tip needle such that it can be inserted within in any tissue under a motion which can be characterized by a time-dependent diffeomorphism. We then explore motion planning under periodic motion of a homogeneous, planar tissue where we use the Rapidly-exploring Random Trees (RRTs) method with the developed model to explore the tissue. While we perform the planning, we aim that the needle reaches a target area in the tissue while avoiding *obstacles* which are actually tissue segments that we want to avoid getting in contact with and intuitively follow the same motion of the tissue.

Keywords: Needle steering, minimally invasive surgery, path planning, kinematic modeling, RRT.

ÖZET

HAREKETLI DOKUDA ESNEK IĞNE INSERSIYONUNUN MODELLENMESI

Aslı Deniz Güven
Bilgisayar Mühendisliği, Yüksek Lisans
Tez Yöneticisi: Asst. Prof. Dr. Selim Aksoy ve Asst. Prof. Dr. Uluç Saranlı
Ağustos, 2012

Yönlendirilebilir iğneler minimal invaziv cerrahi içerisinde daha önce sabit iğneler ile ulaşılması mümkün olmayan klinik hedeflere ulaşmak için kullanılabilirler. Minimal invaziv cerrahide bu tip esnek, yönlendirilebilir iğnelerin bir insersiyon için kullanımı, anatomik engellerin bulunmasının yanısıra iğne hareketinin holonomik olmayışı sebebiyle de oldukça güçtür. Bu çalışmada biz, bu tür cerrahi içerisinde görülen bir diğer özelliği, dokunun kendi hareketini de göz önünde bulundurarak bu insersiyon problemini ele alıyoruz. Örneğin, bir minimal invaziv kalp ameliyatı esnasında kalp atışlarının ya da bir başka cerrahi işlem sırasında nefes alıp verme hareketinin iğne üzerindeki etkileri insersiyonu gerçekleştirecek kişi tarafından göz önünde bulundurulması gereken doku hareketlerindendir. Bu tez dahilinde biz, hareketi zamana bağlı bir difeomorfizm ile tanımlanabilen dokularda gerçekleştirilen iğne insersiyonunun hareket modelini geliştiyor ve bu model ile birlikte kullandığımız bir planlama yöntemi ile, RRT, periyodik bir harekete sahip olan, homojen ve iki boyutlu bir doku için hareket planlaması gerçekleştiriyoruz. Bu planlamayı yaparken amacımız, iğnenin doku içerisinde belirlenmiş hedef bir bölgeye ulaşması ve bunu yaparken de yine aynı dokuya ait, dolayısıyla doku ile aynı harekete sahip bölümlerine, yani *engellere*, iğnenin temas etmemesidir.

Anahtar sözcükler: Yönlendirilebilir iğneler, minimal invaziv cerrahi, yol planlaması, kinematik modelleme, RRT .

Acknowledgement

I would like to express my sincere gratitude to my supervisor Asst. Prof. Dr. Uluç Saranlı for his guidance and his understanding throughout the process of writing this thesis. I thank to him for helping me keep going at the times that I have found it difficult to do so. He has shown me his way of looking at the problems at hand; focused, systematic, and lucid - and have taught me more than just the knowledge of this thesis but helped me build a solid ground which. For all of this, I thank to him.

I am thankful to Asst. Prof. Dr. Selim Aksoy, Assoc. Prof. Dr. Cenk Çavuşoğlu and Asst. Prof. Dr. Çiğdem Gündüz Demir for kindly accepting to be in my commitee and for giving their time to read and review this thesis. I am also grateful to Assoc. Prof. Dr. Cenk Çavuşoğlu for his valuable suggestions and his encouragement during this thesis.

I would like to thank to all of my friends and my office mates for their friendship and support. Without their motivation and energy, it would have been a more difficult task to keep this research going.

Finally, I would like to thank to my family who have been there for me at all times and never stopped believing in me. With very special thanks, I dedicate this thesis to them.

Contents

List of Figures

Chapter 1

Introduction

1.1 Motivation

Advancements in surgery have focused on minimizing the invasiveness of surgical procedures, in which surgeons operate through smaller openings hence reducing the pain and trauma, yielding fast recovery times and thereby shorter hospital stay for the patients who undergo these surgeries [5, 18, 20, 17]. However, along with its advantages, minimally invasive surgery (MIS) has some drawbacks including reduced sight and direct eye coordination. During recent years, several minimally invasive robotic systems (MIRS), such as the daVinci^{TM} system from Intuitive Surgery Inc.[10] and Zeus^{TM} from Computer Motion Inc.[9], have been developed, capable of overcoming various challenges faced by surgeons. These systems are open to use preoperative planning data, they increase precision and also they make new surgery techniques possible, such as minimally invasive beating heart surgery [20].

In addition to their use in MIRS systems, steerable needles have the potential to enable entirely new MIS procedures by allowing needles to reach previously inaccessible locations of the body [12]. Needles with tip asymmetry are steerable since they deflect upon insertion into soft tissue [26]. There are three types of tip asymmetry which makes the needle steerable: bevel, pre-bend, and pre-curve [26] as shown in Figures 1.1.a, 1.1.b and 1.1.c, respectively. All of these steerable needles travel in curved paths within the body. Therefore, they can be steered to

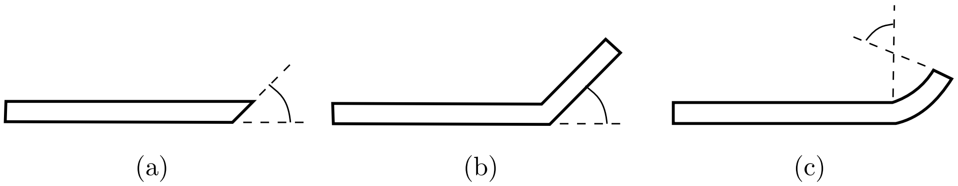

Figure 1.1: Al illustration of three types of tip asymmetry: (a)bevel, (b)pre-bend, (c) pre-curved.

reach some pre-defined locations while avoiding contact with the others by simply traveling around them.

According to [26], bevel-tip flexible needles are the most studied steerable needles. They were developed by Webster and his colleagues, characterized as steerable needle due to their nature of following a curved path depending on the bevel-angle [12, 13]. Using these bevel-tip needles to perform a manual insertion in MIS is a difficult task not only because of the presence of anatomical obstacles and reduced sight but because manually steering these flexible needles is challenging due to the complexity of the needle path as well as the limitations of human manual controls under the kinematic constraints originated by the shape of the needle. Perceptual demands on surgeons for dealing with these difficulties are high, which is the primary reason for robotic devices to control the insertion of these needles with higher precision.

When it comes to autonomously controlling a steerable needle with a robotic device, a needle model should be derived so that the needle controller can predict and plan the insertion. When the first flexible needle model was developed, a kinematic model for needle insertion within a rigid, homogeneous and planar tissue was also introduced [12]. This was, in their own words, the first step toward active needle steering.

In a real needle insertion during a minimally invasive surgery, there are many things to consider: The deformation of the soft tissue when the needle is pushed within, the torsional friction between the needle and the tissue, effect of respiration and for instance in a minimally invasive cardiac surgery the effect of the heart beating. Following Webster's first model, many other researchers have developed kinematic and mechanical models to address cases such as soft tissue deformation [2, 11], torsional effects [25] and others, which we will later describe in Chapter

2 in more details. This made it possible for the planners, whose aim is to find a sequence of needle controls to steer it to a desired location while avoiding the anatomical obstacles, to be applicable for needle insertion.

1.2 Problem Statement & Contributions

This thesis explores the modeling and planning for a bevel-tip, flexible needle, considering needle insertion for more realistic scenarios for minimally invasive cardiac surgery. We take into consideration the periodic motion of the tissue due to effects such as heart beating or breathing, and develop a kinematic needle model applicable for these scenarios. In fact, the kinematic motion model that we develop in this work is applicable for a bevel-tip needle insertion within a tissue whose state, as we will describe in Chapter 3, can be captured by any known diffeomorphic mapping. We leave this mapping non-specific increases its applicability, which we illustrate with different examples of tissue movements. For instance, as in the work of Webster *et al*, the tissue state which is rigid and stationary can be captured by the mapping, or it can capture a state in which the tissue stretches linearly with time, or as we have mentioned, the mapping can represent the state of the tissue in a minimally invasive cardiac surgery where it stretches back and forth in time. After we present the kinematic motion model for a flexible, bevel-tip needle, we then present a sampling-based motion planner based on the Rapidly-exploring Random Trees (RRTs) to quickly explore 2D environments with obstacles and obtain a feasible insertion path with the shortest length.

The main contribution of this thesis is hence a 2D kinematic motion model for the insertion of a bevel-tip flexible needle within a tissue undergoing a time-dependent deformation. To the best of our knowledge, previous work in needle steering and planning considered only rigid tissue insertion for both planar(2D) and general(3D) problems as well as deformations within soft tissues, but have not addressed any tissue motion in modeling and planning. Therefore, we propose the first kinematic needle model which is applicable to needle insertion under such tissue motion. Other minor contributions include modifications to the RRT algorithm so that it quickly explores the environment by expanding for all possible needle orientations at once, and an extension of the RRT algorithm to consider time as part of the needle configuration.

1.3 Thesis Organization

The thesis chapters are organized as follows:

Chapter 2 : Prior work on the topic of tissue modeling, needle modeling and path planning for steerable needles are presented in this chapter.

Chapter 3 : This chapter describes our proposed kinematic model for a bevel-tip, flexible needle for various tissue states including one where the tissue is under a periodic motion as one is in a minimally invasive cardiac surgery. Restriction are that the tissue we model the insertion within is an homogeneous, planar one which does not deform due to needle insertion forces. Simulations are presented for the validation of the model.

Chapter 4 : This chapter presents the use of a known planning algorithm, the Rapidly-exploring Random Trees (RRTs), using the kinematic needle model developed in Chapter 3. Multiple simulations are performed for planning in various planning environments.

Chapter 5 : Thesis contributions and results are summarized, and the future directions to improve the modeling are discussed.

Chapter 2

Background & Related Work

In this chapter, we present key concepts of needle insertion and steering in two sections. First, we will present the modeling of needles and tissues in Section 2.1 and then we will present in Section 2.2 the planning algorithms developed for needle insertions which are based on these models.

2.1 Modeling

2.1.1 Tissue Modeling

Modeling of soft, deformable tissues are generally of importance to surgical simulations and trainings, and path planning methods. This section presents an overview of tissue models which have been presented in the literature.

Before we proceed on to prior work in tissue modeling, let us define two key concepts in the methodology of modeling soft tissues: First things is that, continuum mechanics is the study of deformation or motion of a continuous material under the action of forces. And secondly, finite element method (FEM) is a technique which is used to simulate soft tissue deformation by solving the equations of continuum mechanics. FEM is a mathematical method to discretize a continuous problem [28].

Modeling of Linear Elastic Tissues

Even though biological tissues and large deformations will involve non-linear effects, linear elasticity accurately models small deformations [14], such as the ones which occur in needle insertion. The main reason that linear elastic modeling is preferred is because the computational cost is low and equations remain quite simple.

DiMaio and Salcudean presented soft tissue deformation models by measuring planar tissue deformations during a rigid needle insertion in an experimental system [6]. They characterized the relationship between the forces applied to the tissue by the needle and the corresponding deformations using a linear elastostatic model. This model, which is characterized by two parameters, namely Young's Modulus and the Poisson Ratio, was an approximation to predict tissue deformations in planar tissues. In this work, they have mentioned that given a suitable measurement method for 3D tissue deformations, their models and modeling methodology is applicable to 3D without much difficulty. DiMaio and Salcudean were also the first to develop an interactive linear elastic needle and its coupling tissue model [7]. As in their previous work, their models were based on the measurements of planar tissue deformations and the needle insertion forces. They solved the model as a coupled needle and tissue models to account for needle deflection during the insertion. Both in these works of DiMaio and Salcudean, the tissue was represented as a finite element mesh to perform simulations. These works are a fine example of gathering data from an experiment system and approximate the soft tissue deformations by using this experimental data in a not so complicated FEM-based approach.

As DiMaio and Salcudean, Alterovitz *et al* developed a soft tissue model defined by a 2D mesh [2]. They approximated soft tissues as linearly elastic, homogeneous, isotropic materials and they have set the parameters (Young's modulus and Poisson ratio) accordingly. In doing so, they computed the elastic forces using FEM and forces exerted by the needle to find the deformation of the tissue. As a difference to the work of DiMaio and Salcudean, Alterovitz *et al* considered a flexible needle insertion into this deformable tissue. In one of their following work, they extended this model in 3D by representing the tissue as a tetrahedral mesh and again modeling its elasticity by a finite element method [3].

In conclusion, these prior works give examples of considering the deformation problem of a soft tissue as characterizing the tissue as a finite element mesh and then solving the equations of deformation using FEM.

Modeling of non-linear Elastic Tissues

Non-linear elastic models for tissues are a better way to represent human tissues. Ayache *et al* developed a deformable tissue model based on non-linear elasticity and FEM [24]. This model was valid for large deformations thereby solving the problems related with linear elasticity which, as we have mentioned, is accurate for small deformations.

Misra *et al* described the effects of normal forces during shearing of tissue which is a consequence of non-linearity of the material and are not present in linear elastic models [19]. They have pointed out that this normal forces could be significant depending on the tissue type and explored the Poynting effect for myocardial tissue. This effect describes the interaction of both shear and normal forces during shearing.

For further reading, Nealen *et al* presents physically based deformable models in [21] where they cover a wide range of methods to model deformable objects.

2.1.2 Needle Modeling

Devising a model for a needle is to devise a mathematical model of the needle kinematics or mechanics. This is a prerequisite of needle planning, which we will present in the next section, for the planner should know *where* and in which *state* the needle is going to be throughout an insertion.

To date in needle modeling, soft tissue interaction, deformation and needle flexibility have been considered but no prior work have considered modeling needle kinematics or dynamics under tissue motion.

Needle Modeling in Rigid Tissue

Webster *et al* designed and experimentally validated a nonholonomic model for steering a flexible, bevel-tip needle in rigid, homogeneous 2D tissue [12]. The bevel-tip needle was to be steered from the base with two velocity inputs, insertion speed and rotation speed and their kinematic model of the needle was devised for these two inputs with respect to time. They have assumed that the rotation of the needle and its insertion is not to be performed simultaneously. In such a case, they have showed that bevel-rip needles follow a constantly-curved circular path where the curvature depends on a physical property of the needle which is the angle of the bevel.

Using the flexible needle developed by Webster *et al*, Reed *et al* developed a model of needle under the effect of torsional friction [25]. They have shown that some lag can be introduced between the base of the needle and its tip due to torsional friction and have developed their model and a controller for the torsional dynamics to alleviate the angle lag, hence enhancing the steerability of flexible needles.

Recently, Ko *et al* developed a new type of steerable needle: a needle with a programmable-bevel and presented the kinematic model of this needle [15]. The needle is composed of two interlocked segments which are connected to each other with a spacial interlocking mechanism. Based on this unique design, bevel angle of the flexible probe can be changed by simply sliding one segment on the other, creating an offset which determines the bevel angle. Through this, the needle can follow constantly-curved paths of any curvature as long as the segments preserve their position with respect to each other.

Needle Modeling in Deformable Tissue

For an insertion into a soft, planar tissue, Alterovitz *et al* developed a bevel-tip, flexible needle model which specifies its insertion velocity, cutting force required at the tip of the needle and static and dynamic coefficients of friction that exists between the tissue and the needle [2]. As we have mentioned in Section 2.1.1, Alterovitz *et al* modeled the tissue as a 2D mesh in this work and they also modeled the needle as a line segment which was actually denoted by the edges of triangle elements in the deformed tissue mesh. They updated the material mesh in consideration of the needle kinematics given by Webster *et al* [12] and updated the mesh accordingly. In their following work, they carried this work one step further and modeled the needle in 3D [3], climbing one step further towards a real surgical simulation.

2.2 Planning

When planning for needle insertions, goal is intuitively to steer the needle to a target location without touching the anatomical obstacles. This is acquired by searching for a feasible set of needle controls, *a feasible path*, which can drive the needle to that target location. In this section, we present planning algorithms for needle insertions in the area of medical robotics.

Planning in Rigid Tissues

Alterovitz *et al* considered a planning problem for a bevel-tip, flexible needle in 2D where they also introduced uncertainty in motion direction due to differences in patients and difficulty in predicting needle-tissue interactions [1]. They developed a motion planner where they formulated the planning problem as a Markov Decision problem. They introduced uncertainty using probability distributions and calculated the probability of reaching a target location using Dynamic Programming. The introduction of uncertainty to the planning problem clearly increased the problem's similarity to a real surgical insertion where the *planning environment*, in other words a patient's body, can differ from one person to the other and so the effects of the insertions.

Xu *et al* considered the planning problem of steerable needles in 3D [27]. They assumed a rigid tissue which contains spherical obstacles and applied a sampling-based motion planning algorithm, the Rapidly-exploring Random Trees (RRTs), to quickly explore the environment. They also planned for a feasible entry point where they modified the RRT to use backchaining, in other words they reversed the planning problem to find a feasible path from the target to the entry point in the negative control space. Their approach of finding a feasible entry point is important for it surely affects the success of an insertion.

Patil and Alterovitz also developed a planning algorithm to explore a 3D environment assuming a rigid tissue using an RRT [22]. They combined the RRT with a reachability-guided sampling heuristic, relaxed the constraints of constant-curvature trajectories and offered a speed-up of orders of magnitude. With this speed-up they allowed the obstacles to be defined interactively, computing the the motion plans for the updated environment in under 1 second. Their work is an important fact due to its property of being interactive, for they offer instant changes in decision which might actually occur in a surgical operation.

Duindam *et al* presented a different solution to the motion planning problem using inverse kinematics both for 2D and 3D environments along with reachability and path complexity analyses [8], where Lobaton *et al* followed a different approach in path planning for bevel-tip needles: Instead of sampling needle configurations as in standard sampling methods, they sampled constant-curvature circles and generated feasible transitions between these sampled circles [16]. Then they have formulated their problem as finding a minimum directed Steiner tree.

Planning in Deformable Tissues

In planning for a bevel-tip needle within a planar, deformable tissue, Alterovitz *et al* formulated the planning problem as a constrained nonlinear optimization problem [2]. As a result, their algorithm computed locally optimal entry point and orientation, and an insertion distance which can compensate predicted tissue deformations and reach the target. Their planner did not accept a rotation to change the bevel orientation and therefore they applied the planner to the two meaningful orientations in 2D: bevel-right and bevel-left.

Hauser *et al* considered a problem of reaching to a target in 3D deformable tissue, though they did not considered obstacles [11]. They presented a feedback controller which steers the needle along helical paths within the workspace and the control policy for steering the needle was: find the helical path which minimizes the distance to the target. They mentioned that in the presence of simple obstacles, it is possible for the controller to avoid them by simply excluding them from the workspace.

Patil *et al* presented a simulator for soft tissue taking into account the uncertainty in deformation, noisy sensing and unpredictable actuation [23]. They used a sampling based planner along with a simulator to correspond for tissue deformations and generated a set of plans based on the expected deformations. Then they have selected the plan which has the highest estimated probability to avoid obstacles and reach the goal. This work is important for taking into interactions which actually happen in real life, therefore the solution they offer is a one which takes the scope of prior work and extends it closer for applications in real life.

Chapter 3

Modeling Needle Motion in Moving Tissue

3.1 Problem Definition

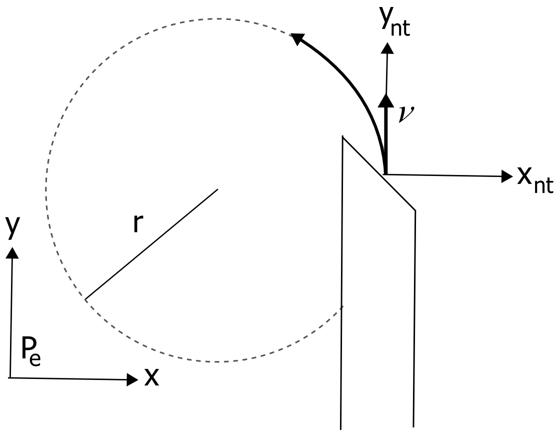

Figure 3.1: An illustration of the bevel-tip needle. Due to asymmetrical forces acting on the needle tip, it follows a circular path of radius r as shown in dashes.

In this chapter, we consider the modeling of a steerable needle inserted into a planar tissue. The needle we take into consideration is a flexible needle with an asymmetric bevel-tip as shown in Figure 3.1. In particular, when the needle is pushed towards the tissue, the bevel tip causes the needle to feel asymmetric forces. This results in the needle bending in the direction of the bevel-tip as it moves further into the tissue.

In modeling the tissue in which the needle is inserted, we consider the possibility of having different physical states at different times. For instance, we would like to model insertion when the tissue is deforming under the effect of breathing with a periodic motion. This model will also comprise the case when the tissue is stationary, reducing the problem to earlier investigations on needle modeling.

To express the different states of the tissue, we define two separate representations. The first representation is the real representation, T_r, which reflects the actual state of the tissue in a given time. For instance, if a tissue under periodic motion is represented in T_r, we would see the tissue motion as we would in real life. We define the second representation to be the canonical representation, T_c, which is a snapshot of the tissue at a specific time. The relationship between these two representations is such that T_c can be mapped into T_r through a time-dependent diffeomorphism. Denoting this diffeomorphism with $\psi : T_c \times \Re \rightarrow T_r$, we can say that any state in T_r can be captured in T_c through ψ. As shown in Figure 3.2, let $\mathbf{p}_c \in T_c$. Then we can define the mapping ψ such that at any time t, $\mathbf{p}_c$ can be mapped to a real point, $\mathbf{p}_r \in T_r$, through ψ. In other words $p_r = \psi_t(p_c)$.

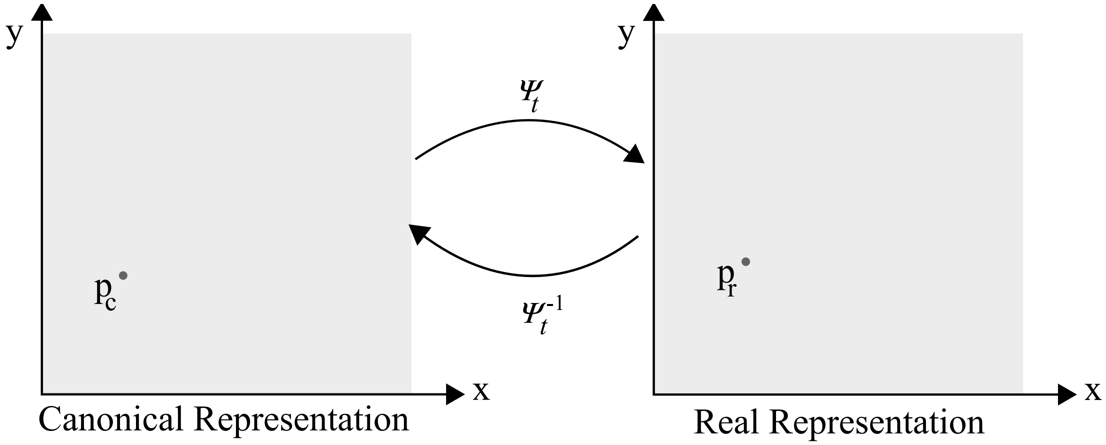

Figure 3.2: An illustration of the tissue in both of its representations. A point $\mathbf{p}_c \in T_c$ is mapped to $\mathbf{p}_r \in T_r$ through the time dependent diffeomorphism ψ.

In conclusion, we state our problem as the modeling of a bevel-tip needle within a planar tissue whose state can be described by a time-varying ψ. If such a mapping exists, then we will devise our needle model in T_c, where the tissue appears stationary with respect to time and using ψ, will simulate the needle insertion in T_r.

3.1.1 Compensation of Tissue Motion

Before we proceed, we should mention an important assumption about our problem. We assume that the tip of the needle is always in contact with the furthest point in the tissue to which it has reached along the way. In other words, we want the needle tip to remain *stationary* with respect to the tissue. When the tissue expands or contracts, the path length of the needle trajectory will change, requiring the driving robot to adjust needle insertion length accordingly. Therefore, we assume that the needle driver compensates the tissue motion by pushing and pulling the needle in synchrony with the tissue motion. This compensation is done by calculating the distance to pull or push the needle. We omit the details of this compensation, which can easily be derived by computing the path integral along the image of the needle trajectory in the real space.

3.2 Needle Modeling in Canonical and Real Tissue Spaces

As we have mentioned in Section 3.1, we would like to derive a motion model for a highly flexible needle with an asymmetric tip as shown in Figure 3.1. In deriving our model, we begin by defining the configuration of the needle. It should intuitively be clear that the progress of the needle as it is pushed into the tissue is primarily determined by the position and the orientation of its tip. Consequently, we define the *configuration* of the needle as the vector $q := [\ x_{nt},\ y_{nt},\ \theta_{nt}\ ]$, where x_{nt} and y_{nt} give the horizontal and vertical positions of the needle tip, whereas θ_{nt} gives the orientation of the needle right at its tip relative to the x-axis in the counterclockwise direction. We also define the tip position in a single vector as $\mathbf{p}_{nt} := [\ x_{nt},\ y_{nt}\ ]$. Then we can rewrite the configuration as $q = [\ \mathbf{p}_{nt},\ \theta_{nt}\ ]$.

In Section 3.1, we described two representations for the tissue and mentioned that we will formulate the needle model in T_c. The model that we describe will be used to predict needle configuration as a function of time based on insertion velocity and needle orientation. Consequently, we need to think of these representations to properly define a configuration for the needle. As they are now T_r and T_c are related in terms of positions through ψ, but a position is not enough to define the configuration for the needle. It denotes the tip position, but as we have mentioned a configuration also holds an angle to denote the tip angle. Therefore we define two new configuration spaces for the needle tip as $\aleph_c := T_c \times S^1$ and $\aleph_r := T_r \times S^1$.

We now define an extended map, $\bar{\psi}$, such that both positions and orientations of the needle tip in $\aleph_c$ and $\aleph_r$ can be associated through $\bar{\psi}$ in these newly defined configuration spaces. We define this new extended mapping $\bar{\psi}$ as, $\bar{\psi} := \aleph_c \times \Re \rightarrow \aleph_r$, $q_r = \bar{\psi}_t(q_c) = \bar{\psi}_t\left(\begin{bmatrix} \mathbf{p}_c \\ \theta_c \end{bmatrix}\right)$.

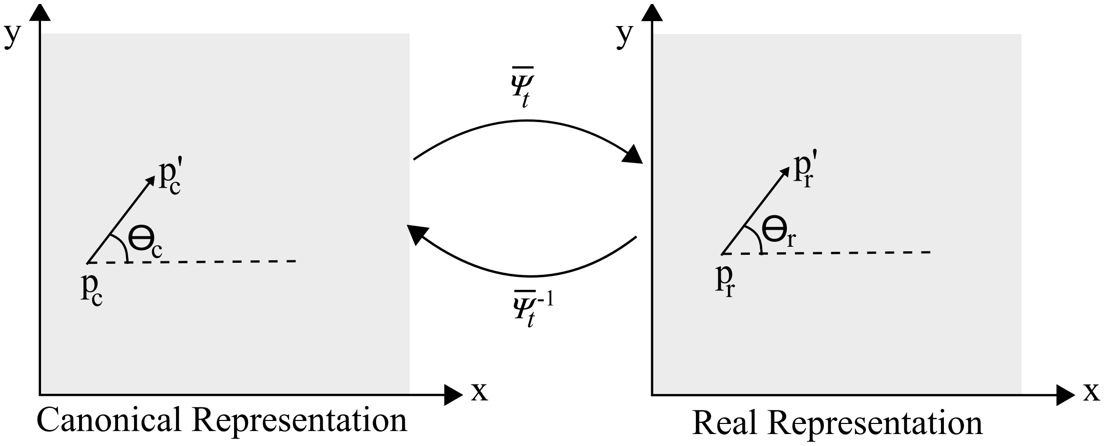

Figure 3.3: An illustration of the two different configuration space representations for the needle. Needle tip in $\aleph_c$ is shown as $\mathbf{p}_c$, whereas needle tip in $\aleph_r$ is shown as $\mathbf{p}_r$. Angles corresponding to the two representations are also shown as θ_c and θ_r. Configuration of a needle is mapped from $\aleph_c$ to $\aleph_r$ by the mapping $\bar{\psi}$.

Intuitively, in this extended mapping $\bar{\psi}$, tip positions can be mapped using ψ. What we need to find is how to relate the angles in $\aleph_c$ and $\aleph_r$. Let us denote the mapping of the angles with ψ_t^a, then we can denote the mapping of configurations in $\aleph_c$ and $\aleph_r$ as follows, $q_r = \begin{bmatrix} \mathbf{p}_r \\ \theta_r \end{bmatrix} = \bar{\psi}_t\left(\begin{bmatrix} \mathbf{p}_c \\ \theta_c \end{bmatrix}\right) = \begin{bmatrix} \psi_{\mathbf{t}}(\mathbf{p_c}) \\ \psi_t^a(\theta_c) \end{bmatrix}$.

Now we can proceed to define ψ_t^a. Let $\mathbf{p}_c$ be the position of the needle tip in

$\aleph_c$. We define another point $\mathbf{p}'_c$ which is obtained by an infinitesimal displacement along the needle direction as shown in Figure 3.3. In other words, for a fixed time t, $\mathbf{p}'_c = \mathbf{p}_c + \Delta\ell \begin{bmatrix} cos(\theta_c) \\ sin(\theta_c) \end{bmatrix}$. Mapping this point to the real workspace we then have

$$\begin{aligned} \mathbf{p}'_r &= \psi_\mathbf{t}(\mathbf{p}'_\mathbf{c}) \\ &= \psi_\mathbf{t}\Bigg(\mathbf{p_c} + \boldsymbol{\Delta}\ell \begin{bmatrix} cos(\theta_c) \\ sin(\theta_c) \end{bmatrix}\Bigg) . \end{aligned}$$

Using a Taylor expansion, we can rewrite $\mathbf{p}'_r$ as

$$\mathbf{p}'_r = \psi_\mathbf{t}(\mathbf{p_c}) + \nabla\psi_\mathbf{t}\Big|_{\mathbf{p_c}} (\mathbf{p}'_\mathbf{c} - \mathbf{p_c}) + \mathbf{H.O.T.} \tag{3.1}$$

$$= \psi_\mathbf{t}(\mathbf{p_c}) + \nabla\psi_\mathbf{t}\Big|_{\mathbf{p_c}} \Bigg(\boldsymbol{\Delta}\ell \begin{bmatrix} cos(\theta_c) \\ sin(\theta_c) \end{bmatrix}\Bigg) + \mathbf{H.O.T.} , \tag{3.2}$$

where H.O.T. stands for higher order terms in the Taylor expansion.

Finally, using the following definition for θ_r and (3.2) we can write

$$\theta_r := \lim_{\Delta\ell \to 0} \angle(\mathbf{p}'_r - \mathbf{p}_r) \tag{3.3}$$

$$= \lim_{\Delta\ell \to 0} \angle\Bigg(\nabla\psi_\mathbf{t}\Big|_{\mathbf{p_c}} \Bigg(\boldsymbol{\Delta}\ell \begin{bmatrix} cos(\theta_c) \\ sin(\theta_c) \end{bmatrix}\Bigg)\Bigg) \tag{3.4}$$

$$= \lim_{\Delta\ell \to 0} \angle\Bigg(\Delta\ell \; \nabla\psi_\mathbf{t}\Big|_{\mathbf{p_c}} \begin{bmatrix} cos(\theta_c) \\ sin(\theta_c) \end{bmatrix}\Bigg) . \tag{3.5}$$

Since we are considering an angle and it is independent of the length of the displacement we can write

$$\theta_r = \angle\Bigg(\nabla\psi_\mathbf{t}\Big|_{\mathbf{p_c}} \begin{bmatrix} cos(\theta_c) \\ sin(\theta_c) \end{bmatrix}\Bigg) = \psi^\mathbf{a}_\mathbf{t}(\theta_\mathbf{c}) . \tag{3.6}$$

This completes the mapping of a needle configuration from $\aleph_c$ to $\aleph_r$. Now, from defining the mapping between representations, we can move on to deriving the needle motion model in $\aleph_r$.

3.3 Modeling Nedle Motion in a Moving Tissue

3.3.1 Notation

Before we proceed to the motion model of the needle, let us first introduce the notation relevant to the derivations. We denote with κ, the curvature of the path which the needle follows if the tissue were stationary. Note that when the tissue is stationary, κ only depends on the physical properties of the needle, more specifically, the bevel angle. Therefore, whenever we mention κ, we mean the curvature which purely depends on the bevel-angle. We then define k, as the curvature of the path which the needle tip follows throughout the insertion within a moving tissue. Naturally, if tissue has no motion of its own, then $k = \kappa$. On the other hand, if the tissue has any non-stationary motion or deformation, then k will reflect the effect of the tissue motion in addition to the stationary κ. In fact, if $\kappa = 0$ then k will only be determined by the tissue motion itself.

In two dimensions, the needle tip can have one of two bevel orientations: left or right. We formalize this observation in the form of a flag, $s \in \{-1, 1\}$ where the values -1 and 1 correspond to left and right orientations, respectively.

Finally, in Section 3.1 we have mentioned that the needle is inserted with constant velocity, we denote the speed of the insertion *relative to the tissue in the real space* by v.

Note that among these, κ and v are assumed to be known a priori since the bevel-angle of the needle is fixed and the insertion speed is controlled by the driver and therefore can be known beforehand.

3.3.2 Motion Model in the Canonical Tissue Space

For a stationary tissue, needle motion can easily be modeled as a constant curvature path [12, 2] with either *bevel-left* or *bevel-right* orientations. But for a time varying deforming tissue, even though κ stays constant for its motion in the tissue itself, k changes since the needle tip is deviated by the motion of the tissue. In other words, both the insertion of the needle and its deviation due to the tissue motion are observed at the same time in $\aleph_r$. In modeling this behavior, we focus on the *instantaneous* motion model where the motion of the needle is defined through the derivative of the needle configuration dq_r/dt at any given time.

In Section 3.2, we defined the map ψ_t^a such that a needle configuration can be mapped from $\aleph_c$ to $\aleph_r$. In this section, we will introduce the motion model for the bevel-tip needle based on these two mappings. As a consequence, we will be able to relate $d\mathbf{p}_c/dt$ and $d\theta_c/dt$ to $d\mathbf{p}_r/dt$ and $d\theta_r/dt$, respectively.

Let us first derive the relation between $d\mathbf{p}_r/dt$ and $d\mathbf{p}_c/dt$. By using the definition of $\psi_\mathbf{t}$, we can write

$$\begin{aligned}\frac{d\mathbf{p}_r}{dt} &= \frac{d}{dt}(\psi_\mathbf{t}(\mathbf{p_c})) && (3.7)\\ &= \frac{\partial\psi_\mathbf{t}(\mathbf{p_c})}{\partial t} + \frac{\partial\psi_\mathbf{t}(\mathbf{p_c})}{\partial\mathbf{p}_c}\,\frac{d\mathbf{p}_c}{dt} && (3.8)\\ &= \frac{\partial\psi_\mathbf{t}(\mathbf{p_c})}{\partial t} + \nabla\psi_\mathbf{t}\bigg|_{\mathbf{p_c}}\,\frac{d\mathbf{p}_c}{dt} && (3.9)\\ &= V_t + V_n^r, && (3.10)\end{aligned}$$

where we identify V_t as the term related to the motion of the tissue and V_n^r as the term related the needle motion in $\aleph_r$, denoting the tip velocity relative to the coordinate frame in $\aleph_r$. As we mentioned in Section 3.1, we assume that the needle is pushed into the tissue at a speed that will maintain a constant velocity for the needle tip in $\aleph_r$. Since this term V_n^r is related to this known constant scalar, which we denote with v, we can obtain $d\mathbf{p}_c/dt$ from the following equality,

$$v\begin{bmatrix} cos(\theta_r(t)) \\ sin(\theta_r(t)) \end{bmatrix} = \nabla\psi_\mathbf{t}\bigg|_{\mathbf{p_c}} .\frac{d\mathbf{p}_c}{dt} \tag{3.11}$$

Renaming the Jacobian for convenience with $J := \nabla\psi_\mathbf{t}\Big|_{\mathbf{p_c}}$, we use it to rewrite (3.11) as

$$v\begin{bmatrix} cos(\theta_r(t)) \\ sin(\theta_r(t)) \end{bmatrix} = J\,\frac{d\mathbf{p}_c}{dt}\ . \tag{3.12}$$

Using the control input v, J and (3.12) we can then obtain $d\mathbf{p}_c/dt$ as,

$$\frac{d\mathbf{p}_c}{dt} = J^{-1}\,v\begin{bmatrix} cos(\theta_r(t)) \\ sin(\theta_r(t)) \end{bmatrix}\ . \tag{3.13}$$

We are now in a position to derive the relation between $d\theta_c/dt$ and $d\theta_r/dt$. Let us define $w_c(t) := \begin{bmatrix} cos(\theta_c(t)) \\ sin(\theta_c(t)) \end{bmatrix}$, to denote the direction of the needle tip in T_c. We can now define $w_r(t) := J(t)\ w_c(t)$ to denote the tip direction in $\aleph_r$. Using w_c and w_r, we can write (3.6) as,

$$\begin{aligned} \theta_r &= \angle(J(t)\ w_c(t)) && (3.14) \\ &= \angle\left(w_r(t)\right) && (3.15) \\ &= atan(w_{r_x}, w_{r_y}). && (3.16) \end{aligned}$$

Using (3.16), we can find $d\theta_r/dt$ as,

$$\begin{aligned} \frac{d\theta_r}{dt} &= \frac{d}{dt}(atan(w_{r_x}, w_{r_y})) && (3.17) \\ &= \nabla atan\left(\frac{\partial J}{\partial t}\ w_c(t) + J\ \frac{\partial w_c}{\partial t}\right), && (3.18) \end{aligned}$$

where

$$\frac{\partial J}{\partial t} = \left.\frac{\partial \nabla\psi_{\mathbf{t}}}{\partial t}\right|_{t,\mathbf{p}_c} + \frac{\partial \nabla\psi_{\mathbf{t}}\Big|_{\mathbf{p_c}}}{\partial \mathbf{p}_c}\ \frac{\partial \mathbf{p}_c}{\partial t}, \qquad (3.19)$$

$$\frac{\partial w_c}{\partial t} = \begin{bmatrix} -sin(\theta_c(t)) \\ cos(\theta_c(t)) \end{bmatrix} \frac{\partial \theta_c}{\partial t}. \qquad (3.20)$$

Defining $u(t) := \begin{bmatrix} -sin(\theta_c(t)) \\ cos(\theta_c(t)) \end{bmatrix}$ and using (3.19) and (3.20) to rewrite (3.18), we have

$$\frac{d\theta_r}{dt} = \nabla atan\left(\left.\frac{\partial \nabla\psi_{\mathbf{t}}}{\partial t}\right|_{t,\mathbf{p_c}} w_c(t) + \frac{\partial \nabla\psi_{\mathbf{t}}\Big|_{\mathbf{p_c}}}{\partial \mathbf{p_c}}\ \frac{\partial \mathbf{p}_c}{\partial t}\ w_c(t) + J\ u(t)\ \frac{\partial \theta_c}{\partial t}\right).$$

We have explained that the curvature of needle motion relative to the tissue, κ, stays constant due to its nature of being dependent only on the bevel-angle and therefore the rate of change of tip's angle due to pure needle insertion is equal to κvs in $\aleph_r$. To obtain $d\theta_c/dt$, we need to find the components corresponding to pure needle motion in (3.21) and set these terms to be equal to this change. Note that the latter two terms in parenthesis in (3.21) multiplied by$\nabla atan$, are the terms related to the needle motion itself and therefore should be set to κ. In other words

$$\begin{aligned}
\kappa v s &= \nabla atan \left(\frac{\partial \nabla \psi_{\mathbf{t}}\Big|_{\mathbf{p_c}}}{\partial \mathbf{p}_c} \frac{\partial \mathbf{p}_c}{\partial t}\, w_c(t) + J(t)\, u(t)\, \frac{\partial \theta_c}{\partial t} \right), \\
&= \nabla atan \frac{\partial \nabla \psi_{\mathbf{t}}\Big|_{\mathbf{p_{c_x}}}}{\partial p_{c_x}} \frac{\partial p_{c_x}}{\partial t}\, w_c(t) && (3.21) \\
&+ \nabla atan \frac{\partial \nabla \psi_{\mathbf{t}}\Big|_{\mathbf{p_{c_y}}}}{\partial p_{c_y}} \frac{\partial p_{c_y}}{\partial t}\, w_c(t) && (3.22) \\
&+ \nabla atan\, J(t)\, u(t)\, \frac{\partial \theta_c}{\partial t}\,. && (3.23)
\end{aligned}$$

Now let us define

$$\begin{aligned}
k_1 &:= \nabla atan \frac{\partial \nabla \psi_{\mathbf{t}}\Big|_{\mathbf{p_{c_x}}}}{\partial p_{c_x}} \frac{\partial p_{c_x}}{\partial t}\, w_c(t), \\
k_2 &:= \nabla atan \frac{\partial \nabla \psi_{\mathbf{t}}\Big|_{\mathbf{p_{c_y}}}}{\partial p_{c_y}} \frac{\partial p_{c_y}}{\partial t}\, w_c(t), \\
k_3 &:= \nabla atan\, J(t)\, u(t).
\end{aligned}$$

Note that k_1, k_2 and k_3 are all scalars. Therefore we have $d\theta_c/dt$ computed as,

$$\frac{d\theta_c}{dt} = \frac{\kappa v s - (k_1 + k_2)}{k_3}\,. \tag{3.24}$$

These derivations complete the instantaneous needle motion model in the canonical space $\aleph_c$.

3.4 Verification of the Model

In Section 3.3 we modeled the motion of the needle in (3.13) and (3.24). In this section, we present simulation results to qualitatively verify this motion model.

3.4.1 Simulation Environment and Parameters

We have used Matlab to implement the motion model and obtain simulation results for needle insertion. In order obtain the needle trajectory, we have used the ode45 Runge-Kutta integrator provided with Matlab. Numerically integrating the differential equations (3.13) and (3.24), we were able to obtain needle configurations in $\aleph_c$ for a needle insertion once the control inputs, namely κ and v, were specified. Having obtained the configurations of the insertion path, we have used $\psi_{\mathbf{t}}$ to obtain the insertion data in $\aleph_r$. The time interval between successive configurations during the integration was kept below $10^{-3}s$ to ensure numerical accuracy.

3.4.2 Insertion with Identity Mapping

When the mapping ψ is identity, i.e. $\psi_{\mathbf{t}}(\mathbf{p_c}) = [\mathbf{x_c},\ \mathbf{y_c}]^{\mathbf{T}} = \mathbf{p_r}$, the motion model given in Section 3.3 should reduce to $d\theta_c/dt = d\theta_r/dt$ and $d\mathbf{p}_c/dt = d\mathbf{p}_r/dt$. In this section, we first give the analytical validation for this reduction and then we present simulation results, for numerical comparison with prior work.

First, let us start with the reduction of $d\mathbf{p}_c/dt$. From Section 3.3 we know that $d\mathbf{p}_c/dt = J^{-1}\ v[cos(\theta_r(t)), sin(\theta_r(t))]^T$ and for an identity mapping, $J = I_2 = J^{-1}$. Therefore, we simply have $d\mathbf{p}_c/dt = v[cos(\theta_r(t)), sin(\theta_r(t))]^T = d\mathbf{p}_r/dt$. For $d\theta_c/dt$, let us find the scalars k_1, k_2 and k_3 given in Equation (3.24). Since there are no terms in J related to the positions in $\aleph_c$ scalars k_1 and k_2 reduce to 0. Therefore we only need to find k_3 which is given as $k_3 = \nabla atan\ J(t)\ u(t)$. As we have stated $J = I_2$ and recall from Section 3.3 that $u = [-sin(\theta_c(t)), cos(\theta_c(t))]^T$, then by substituting the gradient of $atan$ in its place we have

$$k_3 = \begin{bmatrix} \dfrac{-sin(\theta_c)}{cos^2(\theta_c) + sin^2(\theta_c)} & \dfrac{cos(\theta_c)}{cos^2(\theta_c) + sin^2(\theta_c)} \end{bmatrix} \begin{bmatrix} 1 & 0 \\ 0 & 1 \end{bmatrix} \begin{bmatrix} -sin(\theta_c) \\ cos(\theta_c) \end{bmatrix} = 1.$$

This yields $d\theta_c/dt = (\kappa vs - (k_1 + k_2))/k_3 = \kappa vs = d\theta_c/dt$. Due to this reduction configurations obtained in $\aleph_c$ are equal to the ones mapped to $\aleph_r$.

We have performed two insertions with the identity mapping, one for an insertion where the needle orientation is kept constant during the insertion and another where the orientation is changed in the middle. For the first experiment,

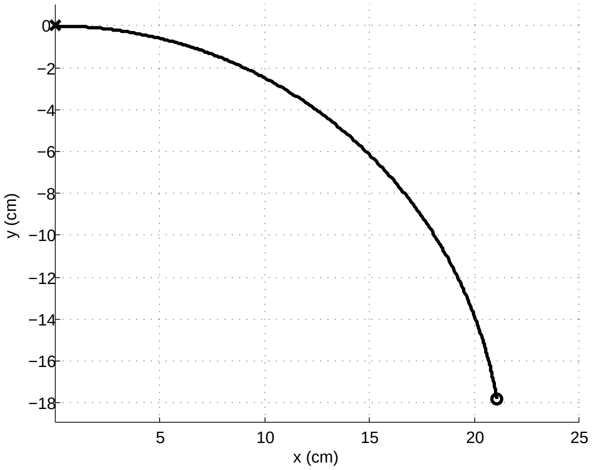

Figure 3.4: An illustration of needle insertion into a stationary tissue with $\kappa = 0.0468$, $v = 1\ cm/s$ and $q_{init} = [0\ \ ,0\ \ ,0]$. Bevel-orientation of the needle is kept constant during the insertion. The needle followed a circular path with radius 21.3cm. The insertion of point of the needle is shown with a cross where the needle-tip is shown with a circle.

we set v to be 1 cm/s and κ to be 0.0468 to simulate the insertion Webster *et al* performed with a needle of the same curvature [12]. Needle was inserted with initial configuration $q_{init} = [0, 0, 0]^T$ and its orientation was kept constant during the insertion. As shown in Figure 3.4, the needle followed a circular arc of radius $21.3cm$ as in the experiments Webster *et al* performed in their work [12].

For the second experiment, we have performed a double-bend insertion where the bevel orientation is changed in the middle of the insertion. We used the same initial configuration, insertion speed and curvature as in the first experiment. The results of this insertion are shown in Figure 3.5 and Figure 3.6. Figure 3.5 shows needle at the end of the insertion and Figure 3.6 (a) and Figure 3.6 (b) show the tip angle and the curvature values throughout the insertion respectively.

3.4.3 Insertion with Linear Constant Tissue Scaling

In this experiment, we simulated the insertion of a bevel-tip needle into a tissue which is stretched to twice of its initial size and into another which is compressed to half of its initial size. Note that the stretching and the compressing of the tissue is done *before* insertion and hence, in terms of needle kinematics, the tissue

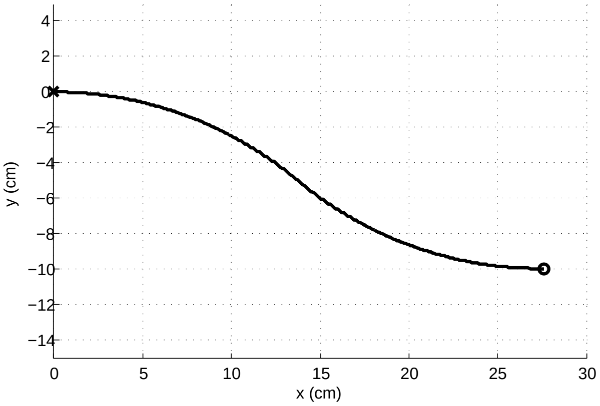

Figure 3.5: An illustration of needle insertion into a stationary tissue with $\kappa = 0.0468$, $v = 1 \; cm/s$ and $q_{init} = [0 \quad ,0 \quad ,0]$. Bevel orientation of the needle is changed from bevel-right to bevel-left in the middle of the insertion. The insertion point of the needle is shown with a cross where the needle-tip is shown with a circle.

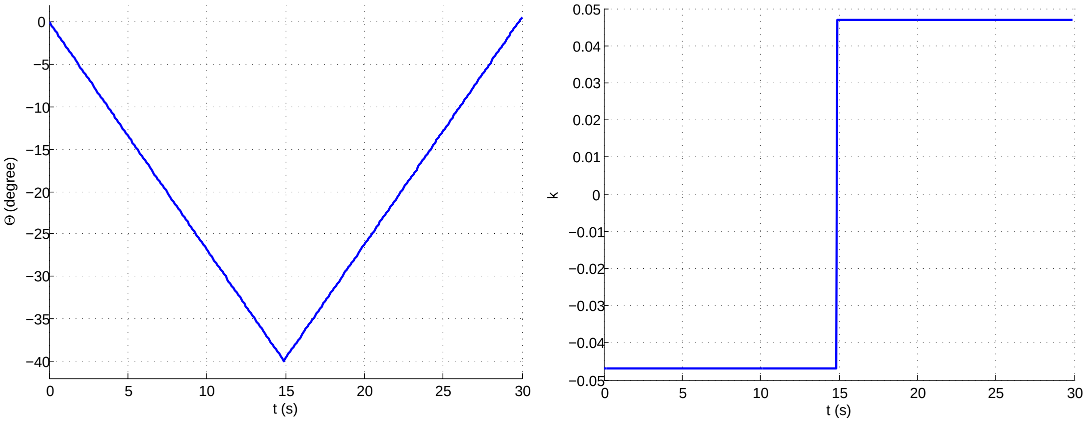

(a) (b)

Figure 3.6: (a) Angle and (b) curvature trajectories for the double-bend insertion plotted as a function of insertion time.

is no different that a stationary one. In other words while inserted into this tissue, the needle should follow a constant-curvature path in $\aleph_r$, since in terms of needle, the tissue is equivalent to a stationary one and the needle is not *aware* of it being in a stretched or compressed state. The state of the tissue is captured in $\aleph_c$ through ψ.

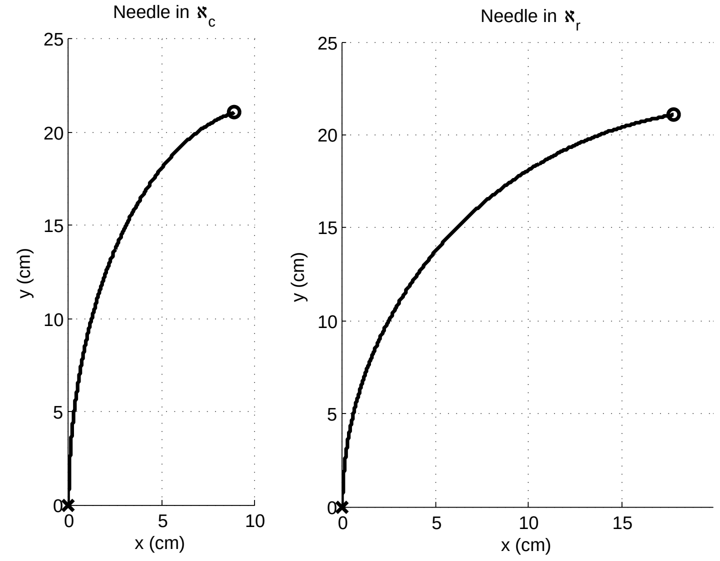

(a) (b)

Figure 3.7: An illustration of needle insertion into a stretched tissue. The needle is inserted into the tissue for 30 seconds with a constant velocity of 1 cm/s, where the needle curvature is set to be 0.0468. The entry point for the needle is shown with a cross where the needle-tip is shown with a circle. (a) shows a snapshot of the needle in $\aleph_c$ at the end of the insertion, whereas (b) shows the needle in $\aleph_r$.

In Figure 3.7, we show the needle at the end of the insertion while the tissue preserves its stretched state. Figure 3.7 (a) shows the view of the needle in $\aleph_c$ and Figure 3.7 (b) in $\aleph_r$, respectively. Note that the needle path in $\aleph_c$ shows the effect of stretching done on the tissue. As we have defined $\aleph_c$ to capture the initial state of the tissue, we could check the validity of this result intuitively. Imagine that we let loose the stretching on the tissue right after the insertion, then with our assumption of the compensation of the tissue motion being present, the needle view would in fact be just like the view as shown in Figure 3.7 (a).

Similar to insertion into a stretched tissue, when the tissue is compressed before the insertion, the canonical representation would then capture the compression in $\aleph_r$ and therefore we should see the needle following a path which is

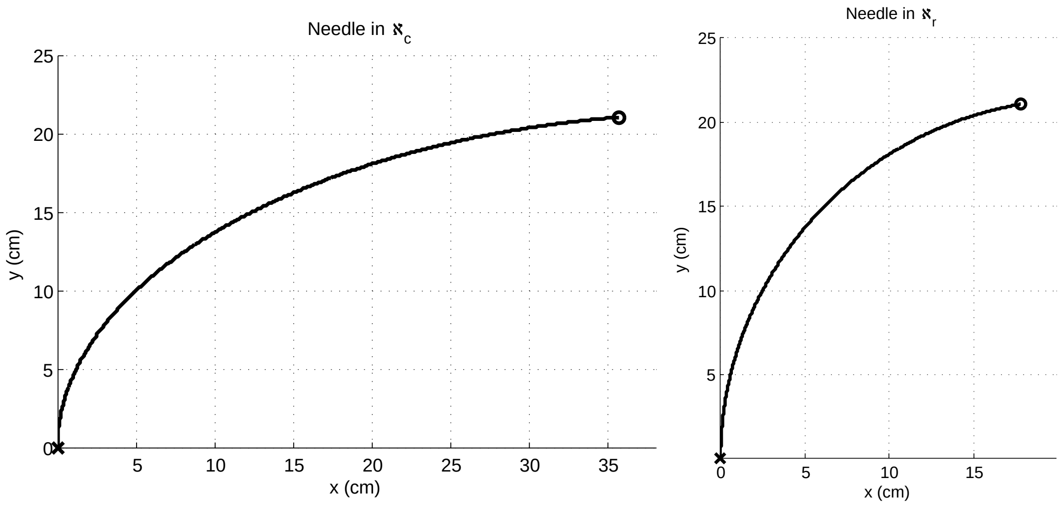

(a) (b)

Figure 3.8: An illustration of the needle insertion into a compressed tissue. Needle is inserted into the tissue for 30 seconds with a constant velocity of 1 cm/s, where the needle curvature is set to be 0.0468. Part (a) shows the needle at the end of the insertion $\aleph_c$ whereas part (b) shows the needle in $\aleph_r$.

wider as shown in Figure 3.8 (a). Again as in the stretched case we can predict the results shown in Figure 3.8 following the idea that if the tissue in $\aleph_r$ is relaxed to go back to its initial state then the view of the needle would be the one as shown in Figure 3.8 (a). Simulation results confirm this intuition, qualitatively verifying that the time-independent parts of the motion model are correct.

In Figures 3.9 and 3.10, we show the angle of the tip throughout insertion for both of expanded and compressed tissue experiments as well as corresponding curvature values for the path that the needle tip has followed. Note that as we have mentioned, whether the tissue is stretched or compressed the needle perceives it as a stationary one. Therefore, the needle view as well as the corresponding tip angles and curvature values in $\aleph_r$ for both of the experiments give the same results. The differences appear for curvature and angle values in $\aleph_c$. Figure 3.9 shows the angle of the tip for both of the experiments in $\aleph_c$ and $\aleph_r$. Note that the values in $\aleph_r$ coincides. Therefore as shown in Figure 3.10 the curvature values in $\aleph_r$ coincides as well.

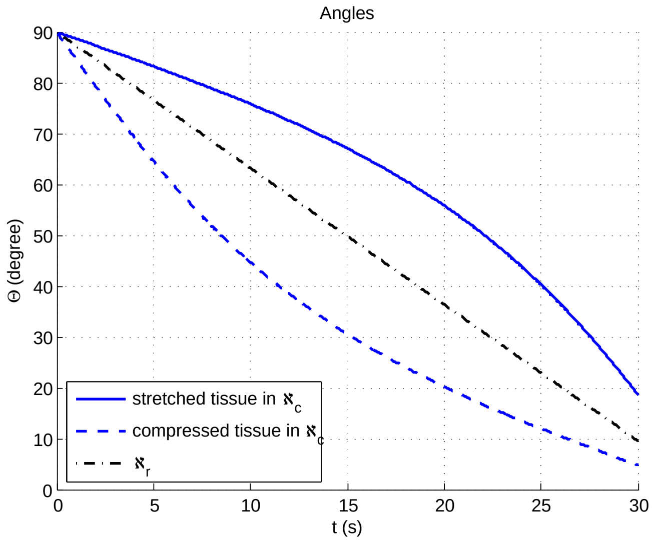

Figure 3.9: Angle of the needle tip throughout the insertion. We display the angle values for the needle in both of the representations, $\aleph_c$ and $\aleph_r$, for an insertion into a stretched tissue as well as an insertion into a compressed one.

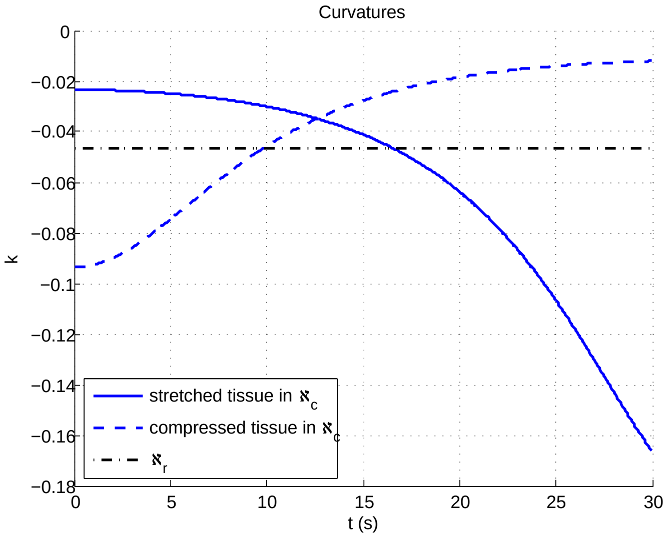

Figure 3.10: Curvature values obtained for insertion into a compressed and a stretched tissue in both $\aleph_c$ and $\aleph_r$.

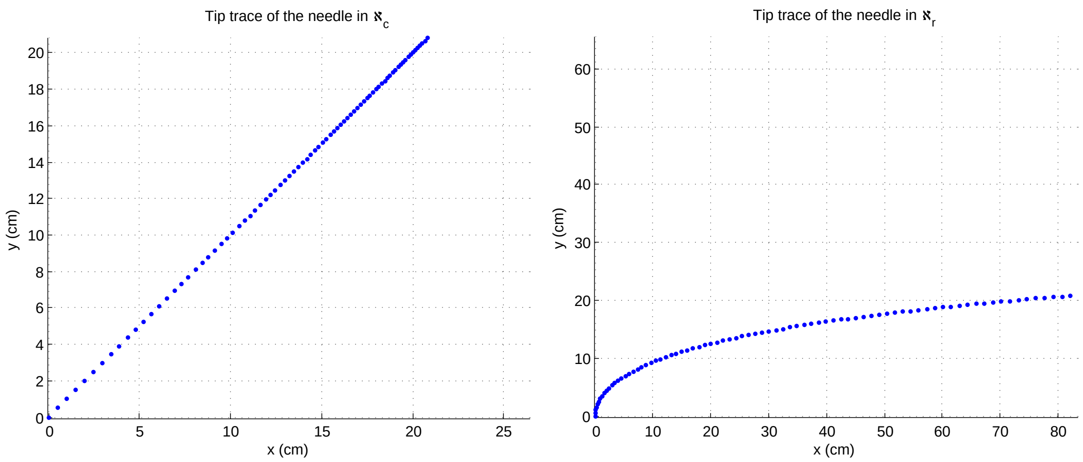

(a) (b)

Figure 3.11: Tip trace of the needle during the insertion.

3.4.4 Needle Insertion for Time Dependent Tissue Motion

3.4.4.1 Linear Motion

As a first test for a time dependent mapping, we simulated needle insertion into a tissue which stretches linearly with time. In other words, we define the state of the tissue with the linear mapping

$$\psi_{\mathbf{t}} : \begin{bmatrix} x_r \\ y_r \end{bmatrix} = \begin{bmatrix} (0.05 + t)x_c \\ y_c \end{bmatrix}.$$

First, we set κ to zero, making the steerable needle a rigid one, and insert the needle with initial configuration $q_{init} = [0, 0, \pi/4]$ into this linearly stretching tissue.

Figures 3.11.a and 3.11.b show the positions followed by the tip of the needle throughout insertion in $\aleph_c$ and $\aleph_r$, respectively. Note that the distance between the positions in $\aleph_c$ decreases, where the ones in $\aleph_r$ gets further away from each other as time progresses. Intuitively, this result shown in Figure 3.11 looks similar to the ones we have obtained in Section 3.4.3. Think of that result we have obtained for the insertion into a stretched tissue, we have seen in Section 3.4.3 that the tissue in $\aleph_c$ reflected the tissue state in $\aleph_r$ by needle configurations which are closer to each other more than they are in T_r. Here, we have something

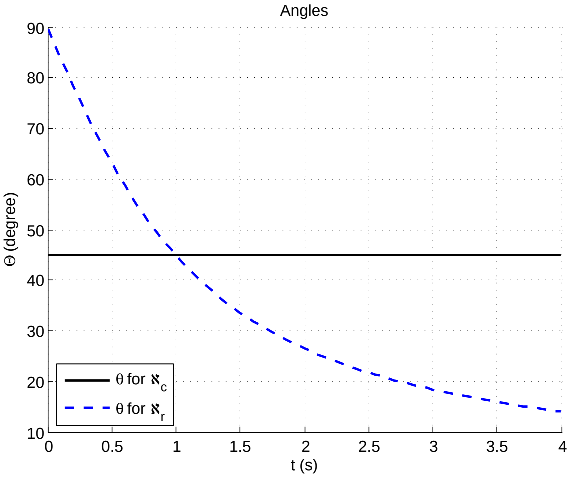

Figure 3.12: Angles of the needle tip throughout the insertion.

similar. Instead of a tissue which is stretched at a constant rate we now have a rate which grows with time. Therefore, as the tissue in $\aleph_r$ get wider and wider, this state of the tissue will be captured in $\aleph_c$ where we see the configurations getting tighter and tighter. Another way to interpret the results shown in Figure 3.11 is that since the insertion speed is kept constant in $\aleph_r$ and Jacobian of the mapping gets larger in time, the correct reflection of the configurations getting farther away from each other in $\aleph_r$ should in $\aleph_c$ be the ones just as shown in Figure 3.11 (a) which are closer to each other. Note that the assumption we have made of the compensation of the tissue is important here, in other words to capture only the effect of the tissue growth we need to make sure that the tip of the needle is kept in contact with the last contact point by the needle driver.

We have shown the values that the tip angle takes throughout insertion and the curvature of the path it had followed, namely k in Figures 3.12 and 3.13, respectively. Note that since the needle curvature is kept constant we have a zero curvature in $\aleph_r$ and the curvature changes in $\aleph_c$ corresponds only to the stretching of the tissue. We have also shown the curvature of the final state of needle in Figure 3.14, note that this reflects the curvature of the needle which is 0.

To make the simulation more clear, we show snapshots from the insertion in $\aleph_r$. Figure 3.15 illustrates the the tip trajectory as well as the view of the needle at different times during the insertion, where the insertion speed of the needle is 10 cm/s all the way through.

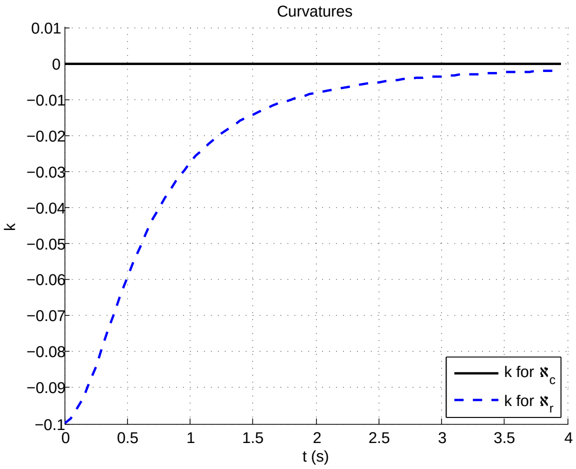

Figure 3.13: Curvature values for the path followed by the needle tip.

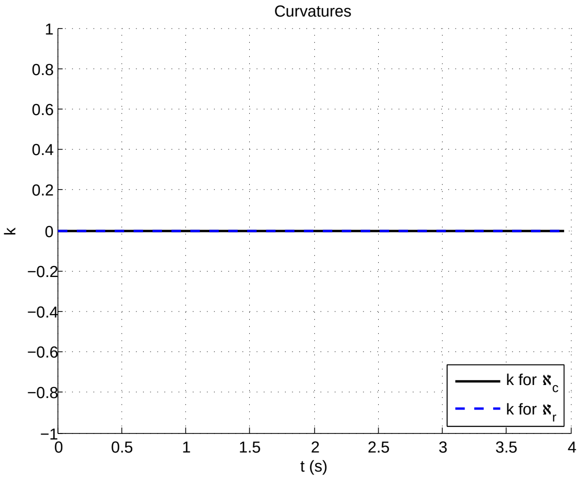

Figure 3.14: Curvature values along the needle body at its final state, at the end of insertion.

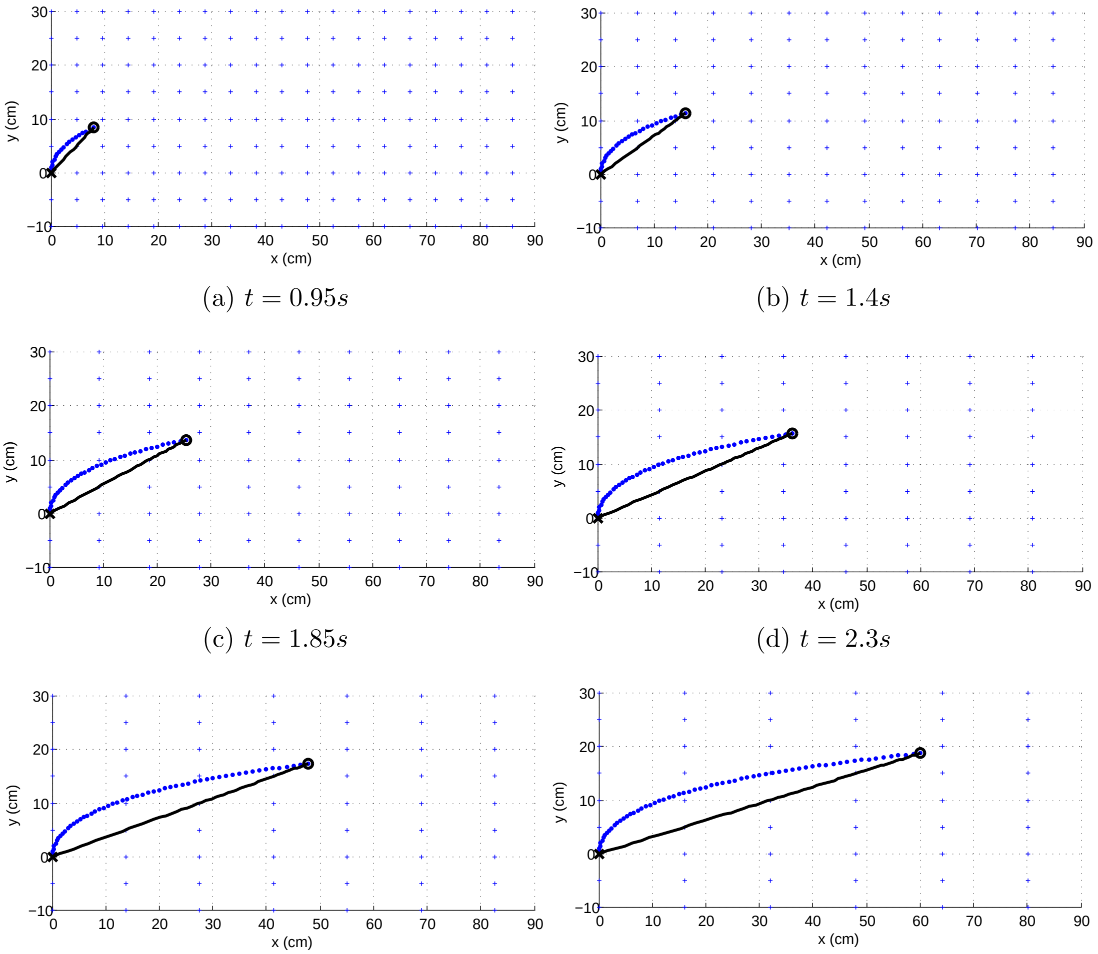

(a) $t = 0.95s$

(b) $t = 1.4s$

(c) $t = 1.85s$

(d) $t = 2.3s$

(e) $t = 2.75s$

(f) $t = 3.2s$

Figure 3.15: Snapshots from a needle insertion into a linearly stretching tissue. Tissue is denoted by blue crosses where the tip trace is shown in blue dots. Needle is shown in a solid black line where the entry point is denoted with a black cross and the needle-tip with a circle. Snapshots are taken in $\aleph_r$ where the needle is inserted with 10 cm/s constant velocity into the stretching tissue.

3.4.4.2 Periodic Mapping

Finally, we have tested our motion model for an insertion into a tissue which is under a periodic motion. As in the linear case, tissue is fixed by one end and is under a motion which stretches and compresses the tissue in a periodic manner. The mapping to capture this motion is

$$\psi_{\mathbf{t}} : \begin{bmatrix} x_r \\ y_r \end{bmatrix} = \begin{bmatrix} (1 + Asin(wt))x_c \\ y_c \end{bmatrix},$$

where A denotes the amplitude and w the frequency of the periodic motion.

As the first experiment, we have inserted a rigid needle with initial configuration $q_{init} = [0, 0, \pi/4]$. The speed for the insertion is set to be 10 cm/s and A and w of the tissue motion to 0.2 and 2 Hz respectively. We show the configurations that the tip have been during the insertion in Figure 3.16 and snapshots from the insertion of the needle are shown in Figure 3.17. The needle is inserted within the tissue for 8 s and note that since we have set w to be 2 Hz we see one full period in $\approx 3s$ as shown in Figure 3.18 where we have displayed the x values of the needle tip in $\aleph_r$.

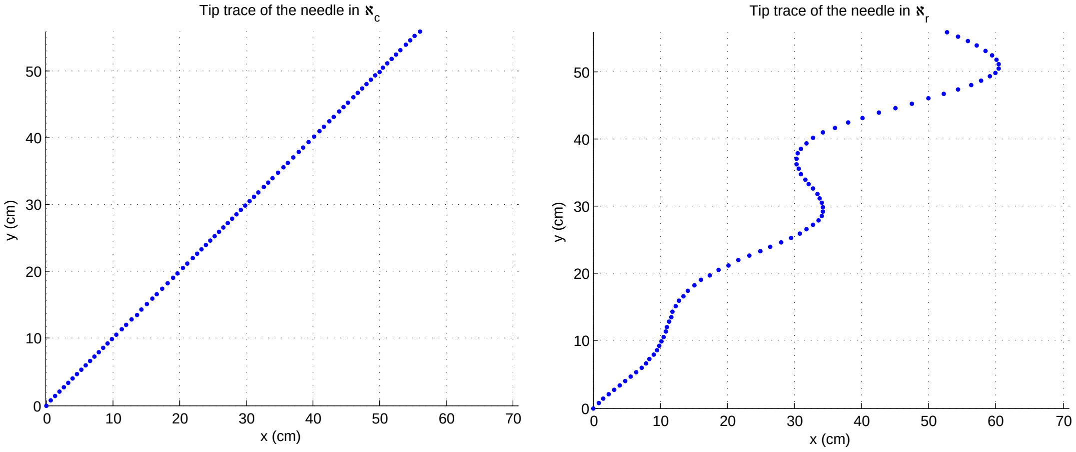

(a)

(b)

Figure 3.16: Tip trace of the needle-tip during the insertion into a tissue under periodic motion. (a) shows the tip trace in $\aleph_c$. (b) shows the tip trace in $\aleph_r$.

As the second experiment we have tested an insertion when the needle curvature $\kappa = 0.0468$. As the initial configuration for this insertion we have set

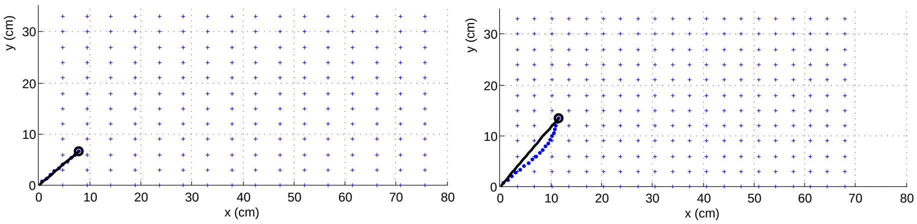

(a) $t = 1s$ (b) $t = 2s$

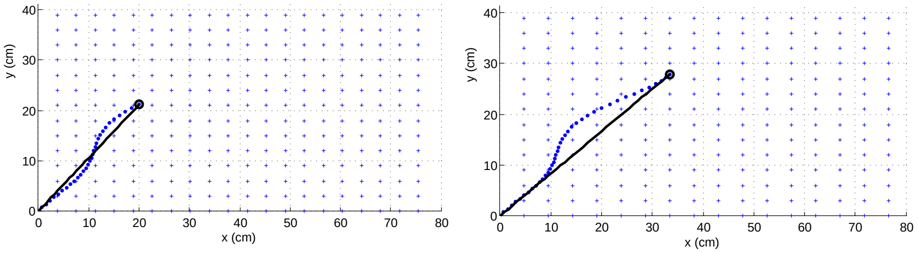

(c) $t = 3s$ (d) $t = 4s$

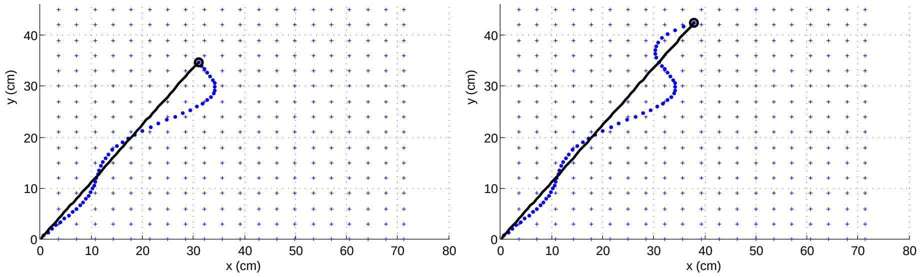

(e) $t = 5s$ (f) $t = 6s$

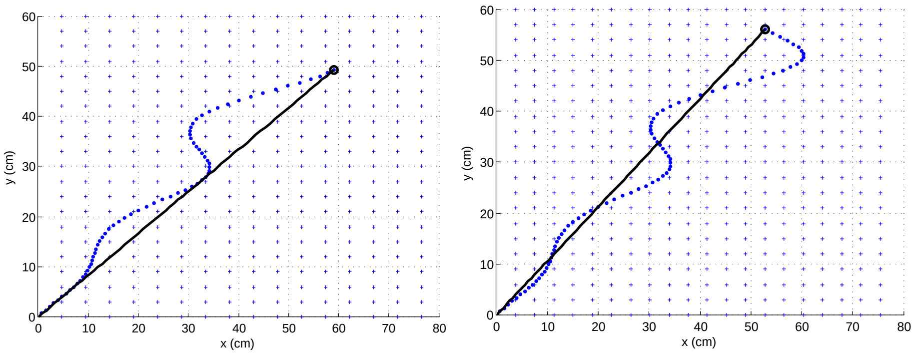

(g) $t = 7s$ (h) $t = 8s$

Figure 3.17: Snapshots taken in $\aleph_r$ where the needle is inserted with 10 cm/s constant velocity for insertion under periodic motion. Tissue is denoted by blue crosses where the path followed by the tip is shown with blue dots and the needle as a solid line.

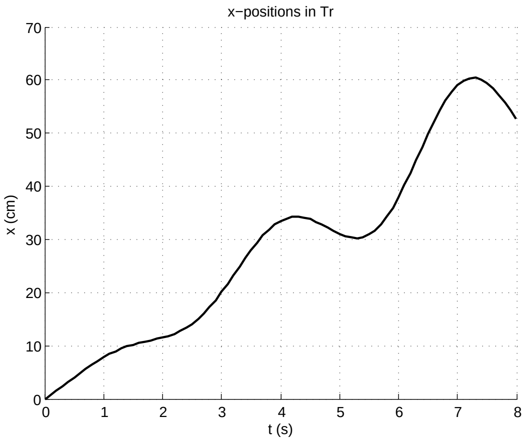

Figure 3.18: x values which are taken by the needle tip in $\aleph_r$ for the insertion under periodic motion.

$q_{init} = [0\ \ ,30\ \ ,0]$. The speed for the insertion is set to be 10 cm/s and A and w of the tissue motion to 0.2 and 2 Hz respectively. We show the configurations that the tip have been during the insertion in Figure 3.19 and the final stated of the needle in both representations in Figure 3.20. The needle is inserted within the tissue for 4 s and note that since we have set w to be 2 Hz we see one full period in $\approx 3s$ as in the previous experiment. We have displayed the angle values of the needle tip throughout the insertion in Figure 3.21 and the corresponding curvature values in Figure 3.22. Finally, we have shown the curvature of the needle body at the end of the insertion in Figure 3.23.

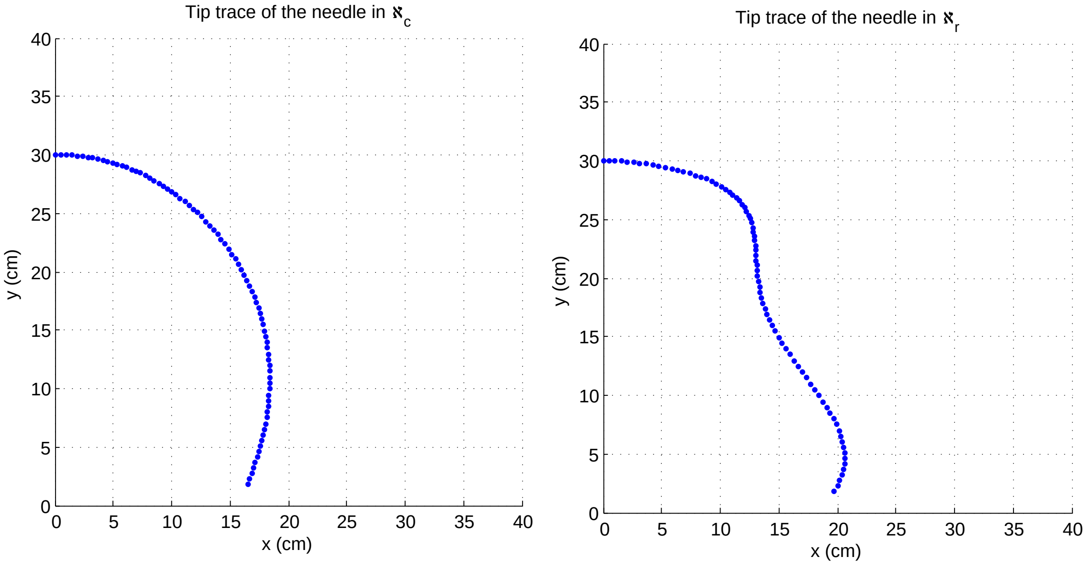

(a) (b)

Figure 3.19: Tip trace of the needle-tip during the insertion into a tissue under periodic motion. (a) shows the tip trace in $\aleph_c$. (b) shows the tip trace in $\aleph_r$.

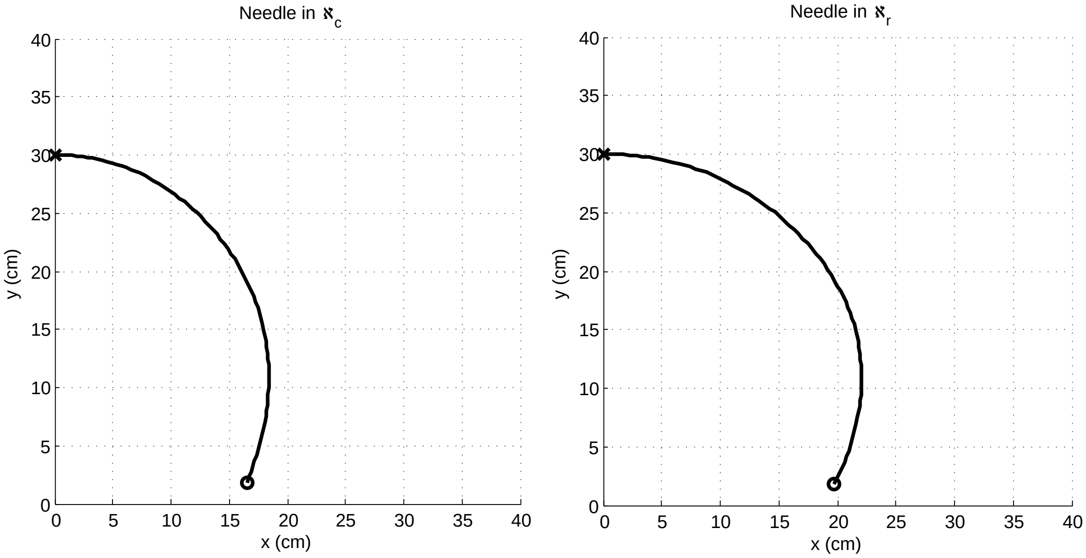

(a) (b)

Figure 3.20: Final view of the needle at the end of insertion. (a) shows the needle view in $\aleph_c$. (b) shows the needle view in $\aleph_r$.

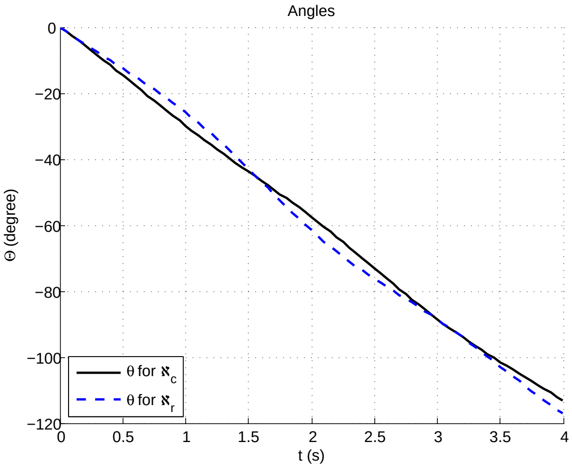

Figure 3.21: Angles of the needle tip throughout the insertion.

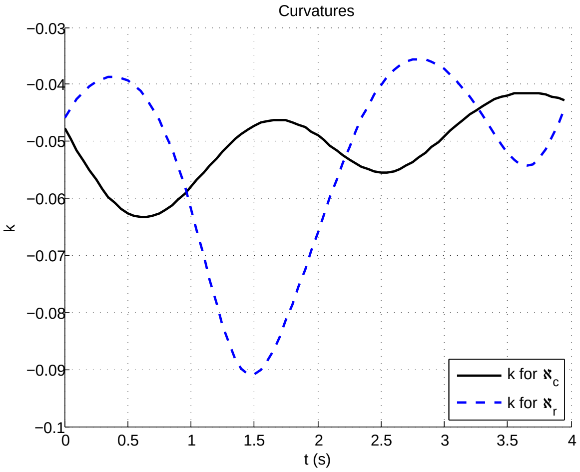

Figure 3.22: Curvature values for the path followed by the needle tip.

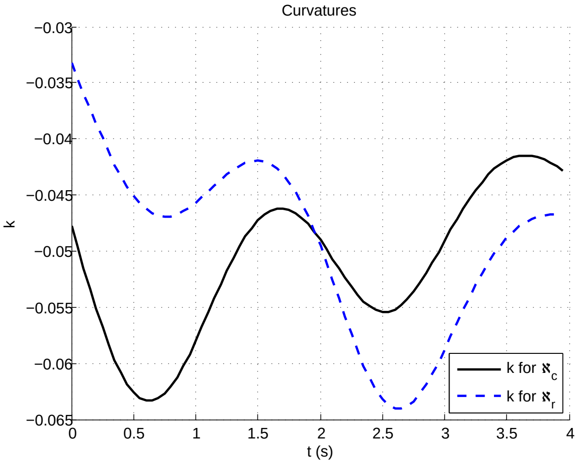

Figure 3.23: Curvature values along the needle body at its final state, at the end of insertion.

Chapter 4

Planning for Needle Motion in Moving Tissue

In this chapter, we consider the problem of motion planning for the bevel-tip flexible needle in a tissue which is under periodic motion. We choose this scenario for the tissue so that it could, for instance, represent the effect of the heart beating during a cardiac surgery, or the effect of breathing in any other procedure with needle insertion. We present the use of a known planning algorithm, the Rapidly-exploring Random Trees (RRTs), using the needle insertion model we have developed in Chapter 3.

4.1 Problem Definition

Since we have derived the needle model in a 2-D space, planning is also considered only in 2-D as well. For the sake of simplicity, we keep the tissue fixed along one side, so the tissue stretches back and forth along one axis. The actual state of the tissue is represented in $\aleph_r$ and $\aleph_c$ represents its idle state. The movement of the tissue is captured by $\psi_{\mathbf{t}} = \begin{bmatrix} (1 + Asin(wt))x_c \\ y_c \end{bmatrix}$ where A denotes the amplitude and w, the frequency of the periodic motion. Obstacles in the tissue are defined to be polygonal, representing segments of tissue which we want the needle to avoid getting in contact with. Due to their nature of being regions from the moving tissue, the obstacles also follow the periodic motion of the tissue. The needle is inserted into the tissue from an initial entry point to reach a target area in the tissue, while avoiding contact with these obstacles. The motion planning problem is to find a sequence of control parameters. For the 2-D case, this is a sequence of bevel orientations and how long they are maintained, such that the needle is guided to the target area.

4.2 Motion Planning Using RRT

Steering bevel-tip needles requires considering nonholonomic constraints: The needle can only be inserted along the tip direction, in other words in the y-direction as shown in Figure 3.1 and not in the x-direction. We chose to use Rapidly-exploring Random Trees since they are suitable for path planning problems which involve nonholonomic constraints.

We will introduce the details of implementing the algorithm later in this section but mainly, we initialize the root node of the tree with the initial configuration of the needle. Then following the RRT algorithm, a reachable, collision-free configuration is randomly sampled to grow the tree from the nearest existing node until the whole space is covered or a number of trials, n, are reached or the tree cannot grow anymore due to the obstacles blocking it way.

Nodes of the tree will contain a needle configuration as well as the time in which that particular configuration is reached during the insertion. For instance, this time property, t_j, for the j^{th} node of the tree will denote the time at which the configuration of the j^{th} node is reached. This property of the node is important to capture the movement of the tissue for this movement is a time-dependent one.

The distance between the nodes is determined by how long the needle is inserted while following a specific orientation. This time in between the nodes is kept constant while the tree is generated and we denote this as t_i. Note that using t_i, we obtain time properties of each node simply by adding it to the parent's time value.

As a planning decision to explore the environment more quickly, when a random configuration is generated and the closest node in the tree is found we generate two children nodes from that node; one obtained by inserting the needle with bevel-right orientation during t_i s and another obtained by inserting the needle with bevel-left orientation during t_i s. Recall that bevel-orientation was captured by a flag $s \in \{-1, 1\}$ where the values -1 and 1 correspond to left and right orientations, respectively.

Having defined the properties of a node in the tree, we now give the algorithm to build an RRT from q_{init}. This algorithm is developed by adapting the RRT algorithm given in [4] to capture the time property of the tissue movement and our decision of growing two children nodes to expand the tree more quickly. Since we have developed the motion model of the needle in $\aleph_c$ the planning also takes place in the same configuration space.

Algorithm 1 Build an RRT from q_{init}

```
procedure BuildRRT($q_{init}$, $n$)
    $T \leftarrow q_{init}$
    for $i = 1$ to $n$ do
        pick $q$ randomly from $\aleph_c$
        Extend(T,$q$)
    end for
end procedure

procedure Extend($T$, $q$)
    $q_{near} \leftarrow$ closest-node($T$,$q$)
    $q_{right} \leftarrow$ motion-model($q_{near}$,$t_{near}$, $-1$)
    $q_{left} \leftarrow$ motion-model($q_{near}$,$t_{near}$, $-1$)
    if $q_{right}$ is collision-free then
        T.add-child($q_{right}$,$q_{near}$)
    end if
    if $q_{left}$ is collision-free then
        T.add-child($q_{left}$,$q_{near}$)
    end if
end procedure
```

Algorithm 1 repeatedly expands the tree T from q_{init} by generating a random collision-free configuration q and growing the tree towards it. While growing the tree from q_{near} towards q, local planner uses the instantaneous motion model developed in Chapter 3 to obtain new configurations q_{right} and q_{left} simply by using two different values of the flag s. Note that when we find the closest node in the tree, q_{near}, to a random configuration, we only look at the Euclidean distance between the positions. At that point, the angle value in that random configuration is not important for the angle of any newly added configuration to the tree only depends on the parent node's tip angle.

Last thing to mention about the implementation of the RRT is that we do not uniformly generate random configurations but instead we generate biased random configurations, where it is guaranteed that in a certain number of generations, a number of configurations will definitely be in the target area.

Last thing to do in the planning is to perform a search for a feasible path in the tree. For this, we have implemented A* search [4] to find the shortest feasible path in the tree, if such a feasible path exists. We have kept the number of trials, n, big enough to ensure wide coverage of the configuration space so that when we would perform A* search to obtain the shortest feasible path in the tree, we would know that this is not a local minimum. In other words, tree is grown wide enough so that there are no nodes which are not expanded and may lead to a shorter path. We have followed such an approach since the motion planning is considered to be a solution to a medical problem and therefore the shortest and fastest solution is the one which would be preferred in those procedures.

4.3 Simulation Experiments

We have tested our planning approach with various experiments where as the first step we have built an RRT in $\aleph_c$ and then searched for the shortest feasible path, if one such path exists. Then if the search returned with such a path, we have mapped the control inputs to $\aleph_r$ and obtained the insertion simulation of the needle in $\aleph_r$ where the movement of the tissue as well as the obstacles are shown as well.

4.3.1 Simulation Environment and Parameters

As in testing the motion model in Chapter 3, we have used Matlab to implement the RRT and obtain simulation results for planning a needle insertion. When generating new nodes to add to the tree we have used our motion model developed in Chapter 3, where we simply generated an insertion of t_i s with initial configuration being the parent node's configuration and s, taking its value depending on which child to generate.

In the experiments we have set the κ and v for the needle as 0.0468 and 1 cm/s, respectively. We have set t_i to be $4s$ and for the amplitude and frequency of the tissue motion we have selected the values 0.2 and $\pi/24$Hz, respectively. We have selected such a frequency value so that the tissue stretches back and forth to reach its idle state in $48s$. This gives in illustrative results with a t_i value of $4s$.

We have generated multiple test environments manually where we have placed the obstacles and the target area within each of the environments by a script we have written again in Matlab.

4.3.2 Experiment with a Single Obstacle

As the first experiment, we have considered planning of an insertion while the target area is blocked by a single obstacle as shown in Figure 4.1.

The tree is generated in $\aleph_c$ with an initial configuration $q_{init} = [0,\ 0,\ \pi/3]^T$. The shortest feasible path found in the tree, as shown in Figure 4.1, is mapped to $\aleph_r$ and there as the tissue moves with time we have the control input sequences denoting which orientation the needle should be at which times. Through this sequence we can control the needle to be driven from q_{init} to the target area, avoiding contact with the obstacle.

Snapshots from the insertion is shown in Figure 4.2 where keep in mind that the assumption of the compensation of the tissue motion we have made in Chapter 3 is present, so that the needle tip preserves its last contact point. This is important we want the needle to stay in the target area once it reaches there.

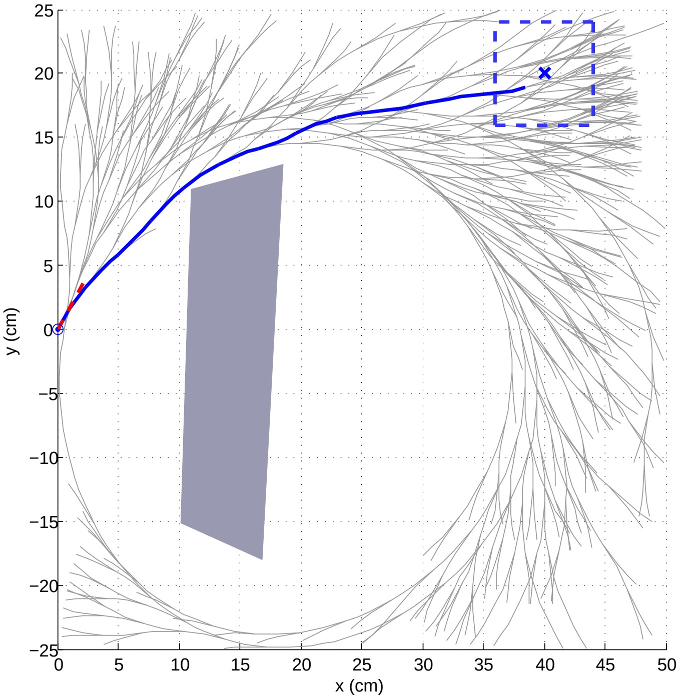

Figure 4.1: An illustration of the RRT generated in $\aleph_c$ after $n = 400$ iterations with $q_{init} = [0\ 0\ \frac{\pi}{3}]^T$. Entry position of the needle is shown with a blue dot and the initial angle with a red, dashed line segment. Target area is shown as a rectangular area with a cross at its center. The path in the tree drawn in blue is the shortest feasible path found to drive the needle from q_{init} to the target.

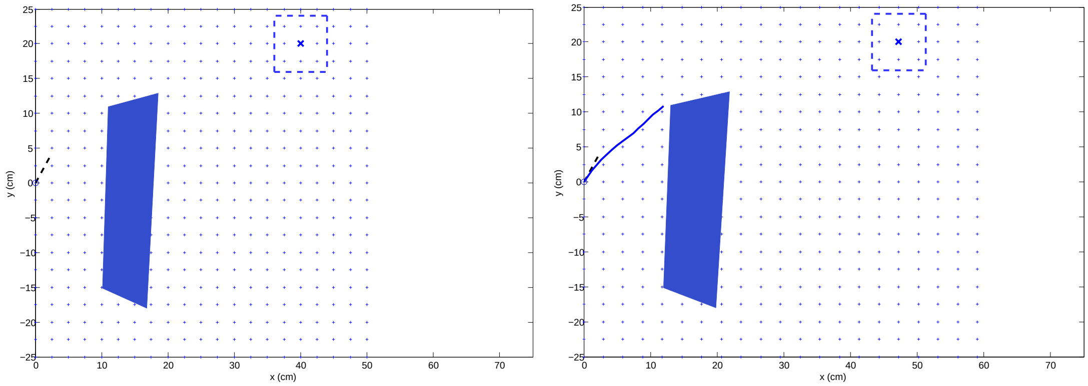

(a) Initial state of the tissue at t=0s (b) t=16s. Tissue stretches forth.

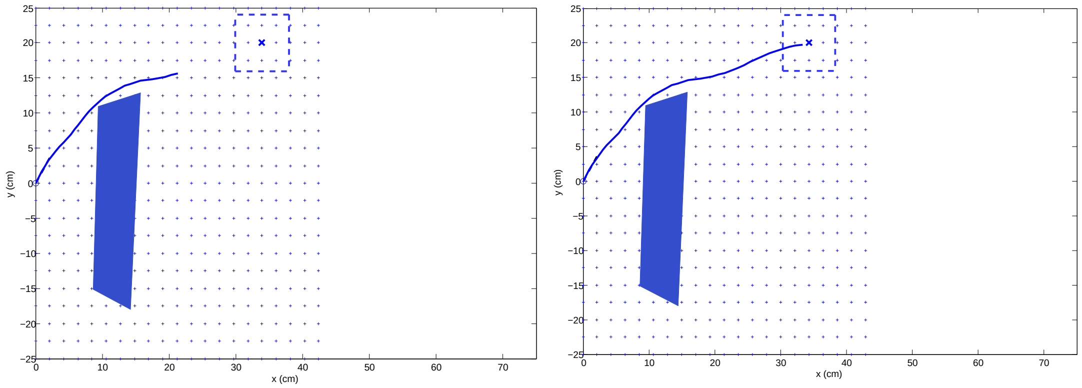

(c) t=32s. Tissue stretches back. (d) t=44s. Target is reached.

Figure 4.2: Snapshots of the needle insertion in $\aleph_r$. Tissue is denoted as blue crosses, target area with a dashed square. We have shown the entry point of the needle with a blue dot and the initial angle with a black, dashed line segment. Needle reaches its target in $44s$.

4.3.3 Experiment with Multiple Obstacles

As the second experiment, we have tested the planner while the target was behind two obstacles. In this experiment, we have tested two different initial configurations where for one of them a feasible path is found and for the other RRT stopped growing due to the presence of the obstacles and therefore the needle did not reach the target.

With $q_{init} = [0,\ 0,\ \pi/3]^T$ the tree is generated in 162 steps and then it stops since it had reached the maximum growth size, in other words there are no configurations to add to the tree since the branches are either blocked by the obstacles or the workspace boundary the algorithm stops and searches for a shortest, feasible path. Figure 4.3 shows the tree after 162 trials as well as the path found to direct the needle to the target area. Snapshots from the insertion are shown in Figure 4.4, where the needle reaches the target area in $\aleph_r$ within $48s$.

In this same experiment, if we change the initial configuration of the needle to be $q_{init} = [0\ 0\ \frac{-\pi}{3}]^T$, then as shown in Figure 4.5 the needle grows for 278 iterations but then it is blocked by the obstacles and the workspace boundary so it stops before reaching to the target area.

This brings out the issue of finding an initial configuration which makes the tree to grow to reach the target or another one to find the *optimal* initial configuration to find the optimal path of shortest length. This is not an issue we have covered in this work, but since the topic occurred here we wanted to mention the problem.

4.3.4 Experiment with Narrow Space

As in the previous example with multiple obstacles we have tested this workspace with different initial configurations. Here, as in the previous example we present a success case and a failure case.

Figure 4.6 shows the tree and the shortest path found when $q_{init} = [0\ 0\ 0]^T$. The tree passes through the gap, covering the area behind the obstacles where the

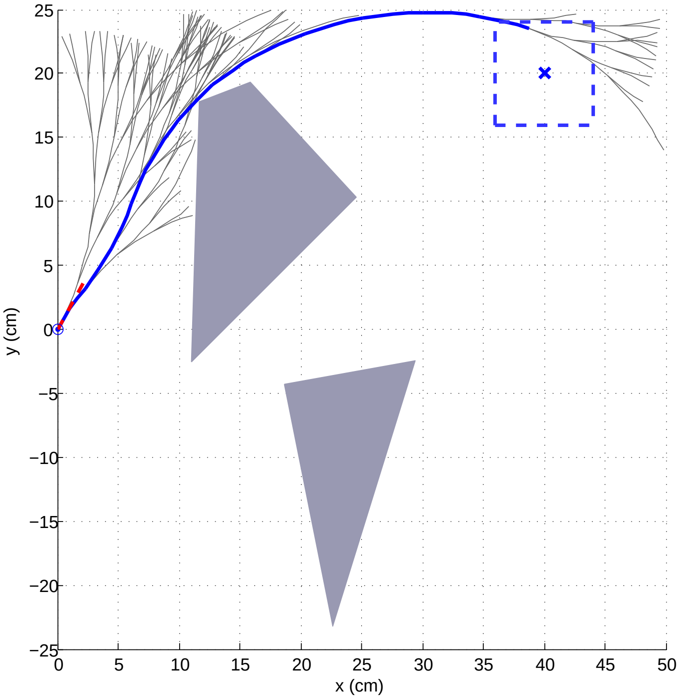

Figure 4.3: RRT generated in $\aleph_c$ in $n = 162$ iterations with $q_{init} = [0\ 0\ \frac{\pi}{3}]^T$. Entry position of the needle is shown with a blue dot and the initial angle with a red, dashed line segment. Target area is shown as a rectangular area with a cross at its center. The path in the tree drawn in blue is the shortest feasible path found to drive the needle from q_{init} to the target.

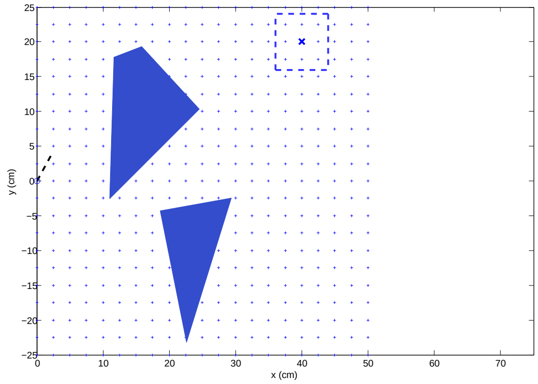

(a) Initial state of the tissue at t=0s

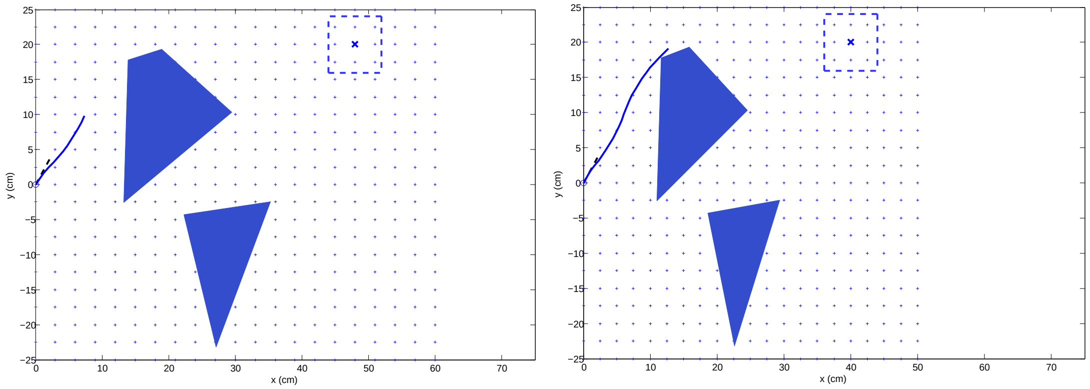

(b) t=12s. Tissue is at its most stretched state. (c) t=24s. Tissue stretches back to idle state.
forth.

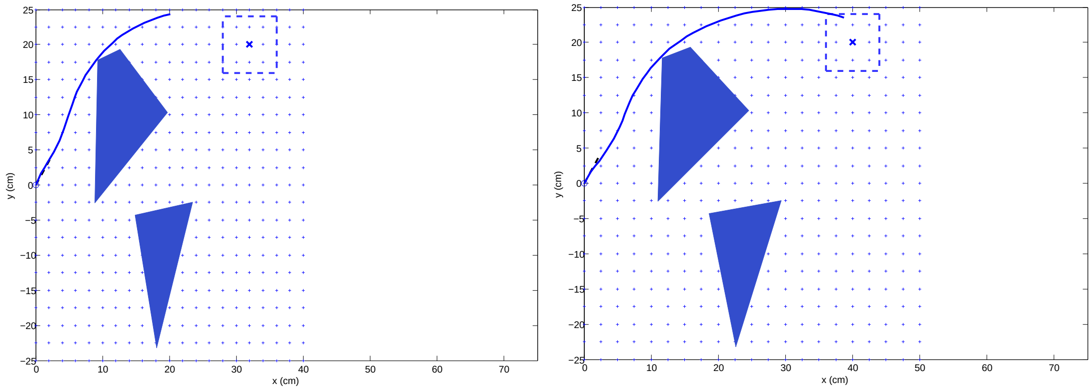

(d) t=36s.Tissue is at its most compressed state.(e) t=48s. Tissue at idle state.Target is reached.

Figure 4.4: Snapshots of the needle insertion in $\aleph_r$ with $q_{init} = [0,\ 0,\ \pi/3]^T$. Tissue is denoted as blue crosses, target area with a dashed square. We have shown the entry point of the needle with a blue dot and the initial angle with a black, dashed line segment. Needle reaches its target in $48s$.

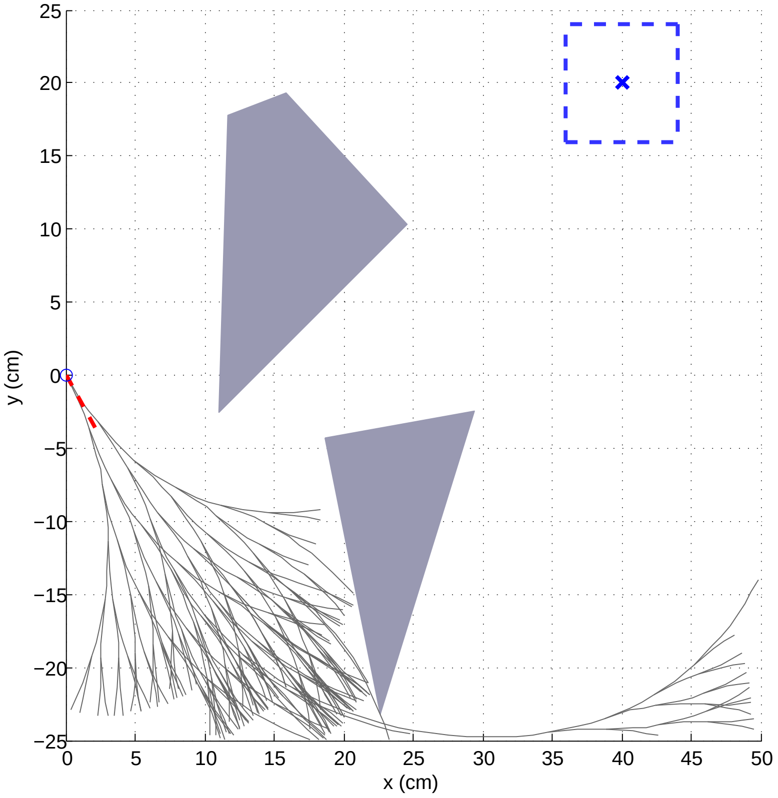

Figure 4.5: RRT generated in $\aleph_c$ in $n = 278$ iterations with $q_{init} = [0\ 0\ \frac{-\pi}{3}]^T$. Entry position of the needle is shown with a blue dot and the initial angle with a red, dashed line segment. Target area is shown as a rectangular area with a cross at its center. Tree is blocked by the obstacles and the workspace boundary before it reaches the target area.

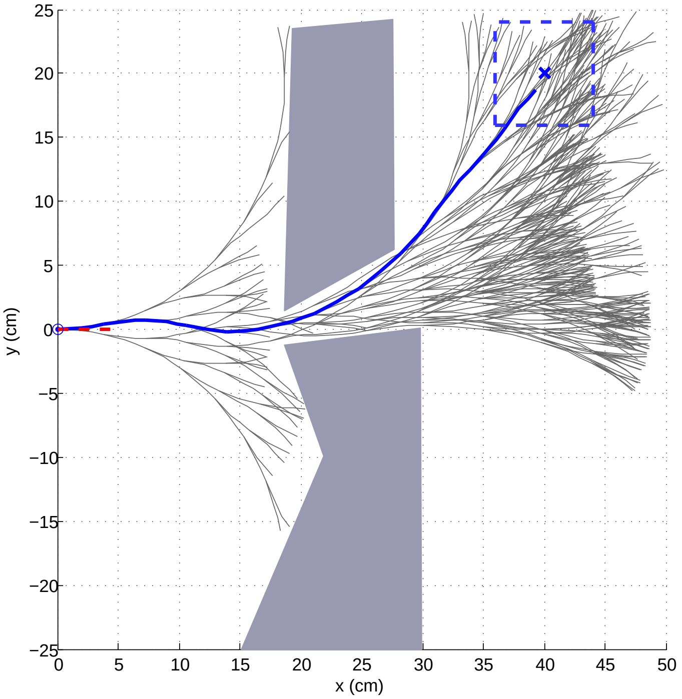

Figure 4.6: RRT generated in $\aleph_c$ in $n = 500$ iterations with $q_{init} = [0\ 0\ 0]^T$. Entry position of the needle is shown with a blue dot and the initial angle with a red, dashed line segment. Target area is shown as a rectangular area with a cross at its center. The path in the tree drawn in blue is the shortest feasible path found to drive the needle from q_{init} to the target.

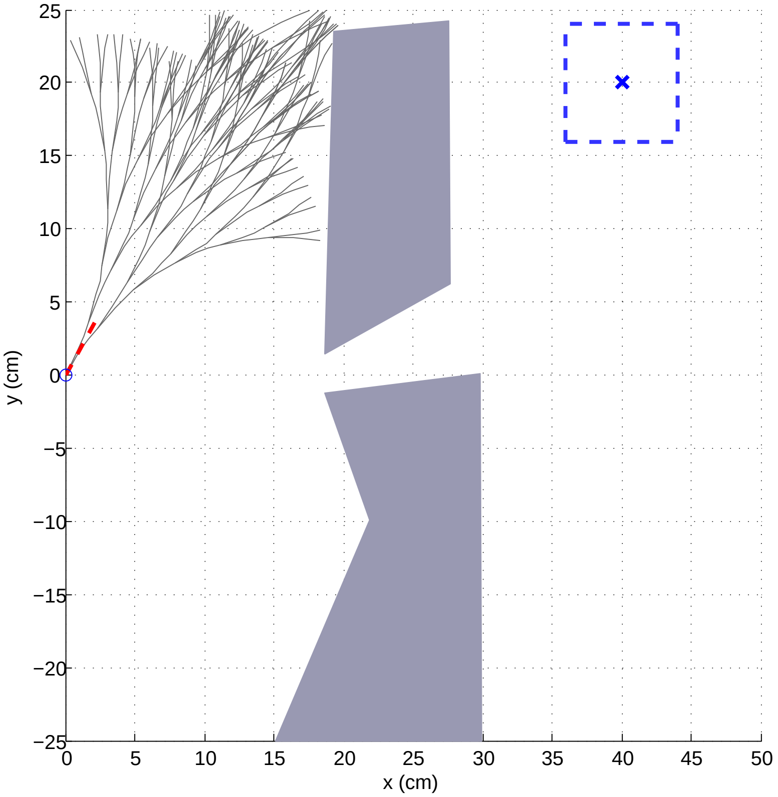

Figure 4.7: RRT generated in $\aleph_c$ in $n = 210$ iterations with $q_{init} = [0\ 0\ \frac{\pi}{3}]^T$. Entry position of the needle is shown with a blue dot and the initial angle with a red, dashed line segment. Target area is shown as a rectangular area with a cross at its center. Tree is blocked by the obstacles and the workspace boundary before it reaches the target area.

target area resides in, in 500 iterations. Though, as shown in Figure 4.7 when we change the initial configuration to be $q_{init} = [0\ 0\ \dfrac{\pi}{3}]^T$, tree stops growing before even reaching the gap between the obstacles.

Snapshots from the insertion in $\aleph_r$ are shown in Figure 4.8 where the needle reaches its target, passing the gap between the obstacles in $48s$.

4.3.5 Experiment with Complex Obstacle

As the final experiment, we have preferred to test the planner with a single, complex obstacle as shown in Figure 4.9. We have placed the target area such that it is covered by the obstacle except one side to increase the difficulty of

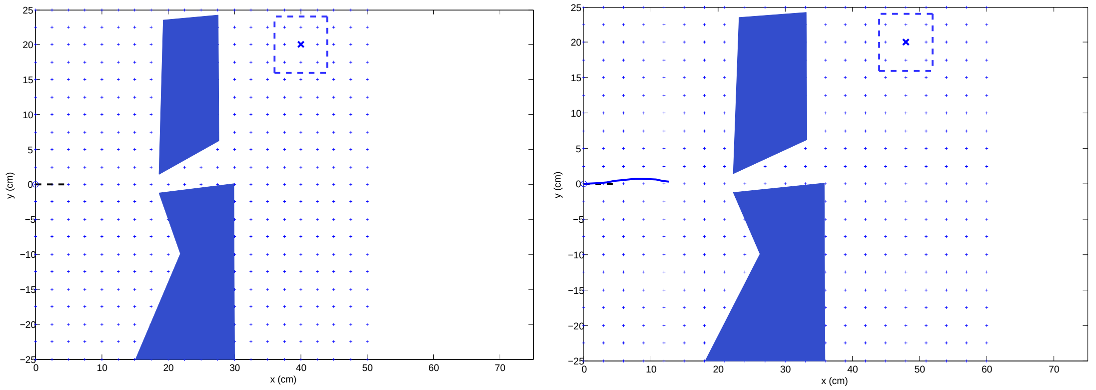

(a) Initial state of the tissue at t=0s

(b) t=12s. Tissue is at its most stretched state. forth.

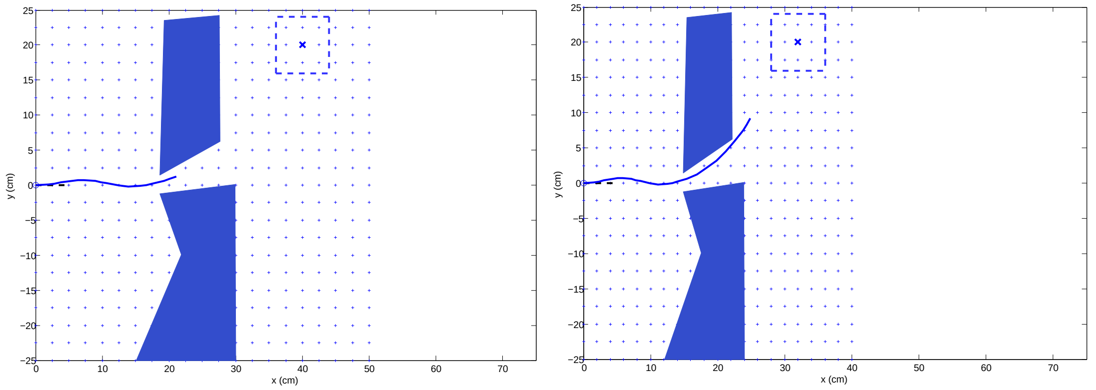

(c) t=24s. Tissue stretches back to idle state.

(d) t=36s.Tissue is at its most compressed state.

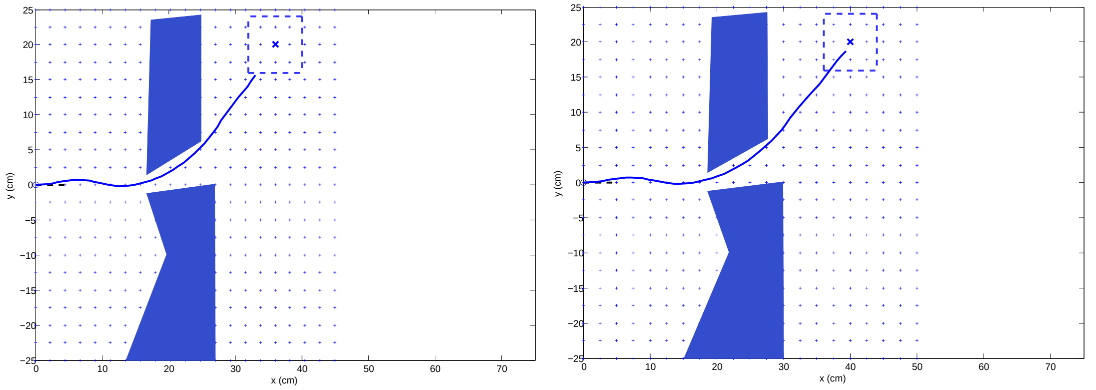

(e) t=44s.

(f) t=48s. Target is reached.

Figure 4.8: Snapshots of the needle insertion in $\aleph_r$ with $q_{init} = [0\ 0\ 0]^T$. Tissue is denoted as blue crosses, target area with a dashed square. We have shown the entry point of the needle with a blue dot and the initial angle with a black, dashed line segment. Needle reaches its target in $48s$.

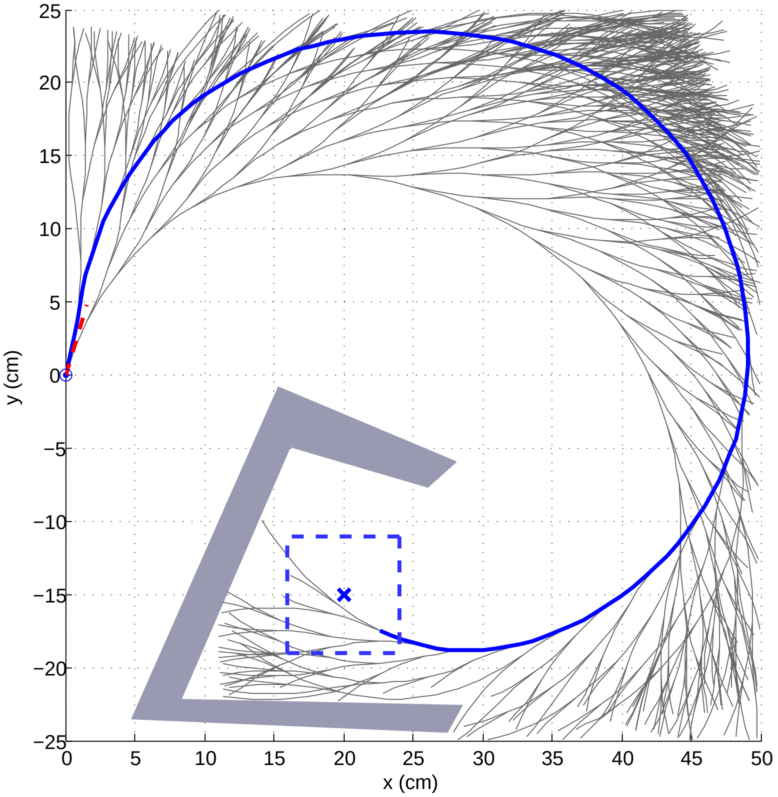

Figure 4.9: RRT generated in $\aleph_c$ in $n = 1000$ iterations with $q_{init} = [0\ 0\ \frac{2\pi}{5}]^T$. Entry position of the needle is shown with a blue dot and the initial angle with a red, dashed line segment. Target area is shown as a rectangular area with a cross at its center. The path in the tree drawn in blue is the shortest feasible path found to drive the needle from q_{init} to the target.

the task. As in the previous cases, selection of the initial configuration plays a part of successfully growing the tree to the target though in this case due to the complexity of the obstacle even the slightest change in the angle effects the result.

Figure 4.9 shows the tree grown in 1000 iterations with $q_{init} = [0\ 0\ \frac{2\pi}{5}]^T$. With this initial configuration tree reaches the target and the path found in it is shown in Figure 4.9 whereas, when we change the initial angle to be $\frac{5\pi}{14}$ then tree cannot reach the target in, again, 1000 iterations as shown in Figure 4.10.

We have shown the snapshots from the insertion in $\aleph_r$ in Figure 4.11 where the needle reaches its target in $112s$. This insertion corresponds to the path found in the tree shown in Figure 4.9, when $q_{init} = [0\ 0\ \frac{2\pi}{5}]^T$. In this case, the needle

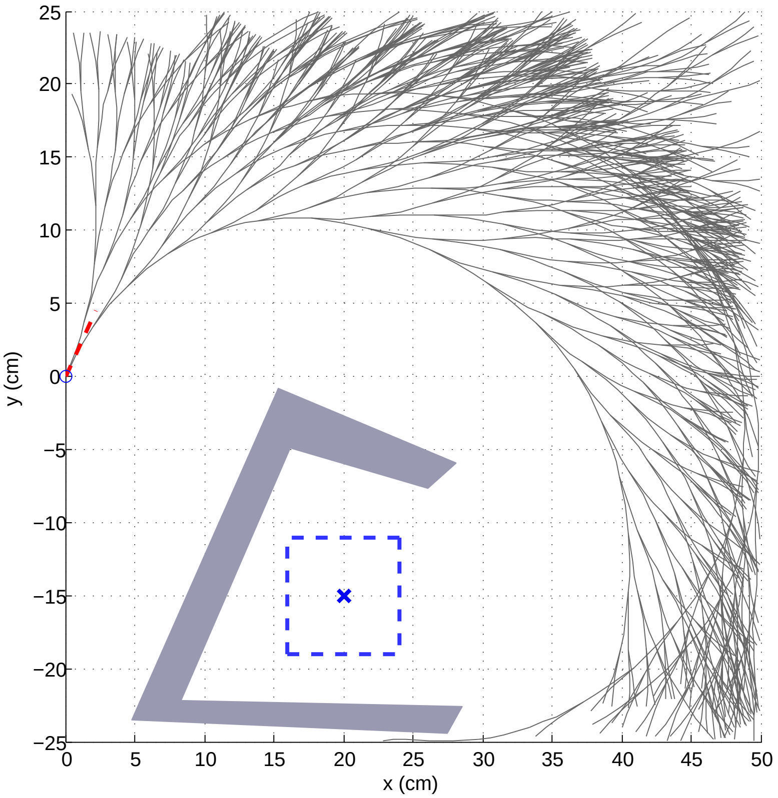

Figure 4.10: RRT generated in $\aleph_c$ in $n = 1000$ iterations with $q_{init} = [0\ 0\ \frac{5\pi}{14}]^T$. Entry position of the needle is shown with a blue dot and the initial angle with a red, dashed line segment. Target area is shown as a rectangular area with a cross at its center. Tree is blocked by the obstacles and the workspace boundary before it reaches the target area.

had one orientation change: Starting from bevel-left orientation as the initial orientation, the needle then changes the orientation to bevel-right after the first $4s$ and preserves it until the end of the insertion.

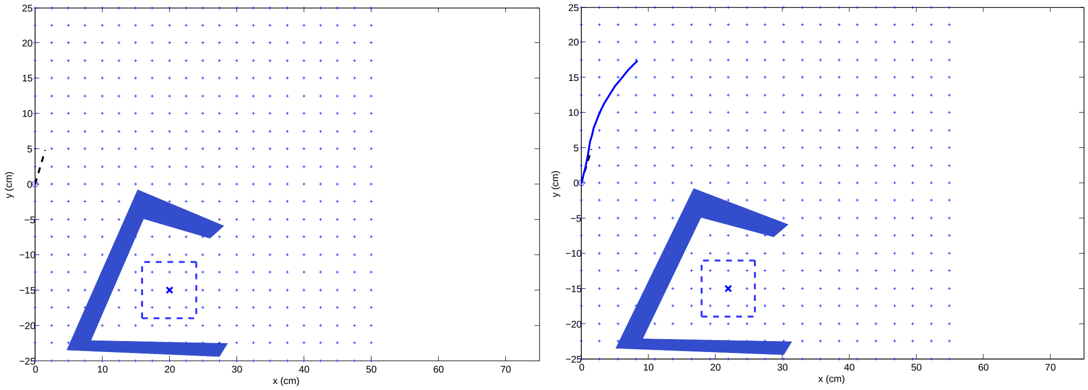

(a) Initial state of the tissue at t=0s

(b) t=20s

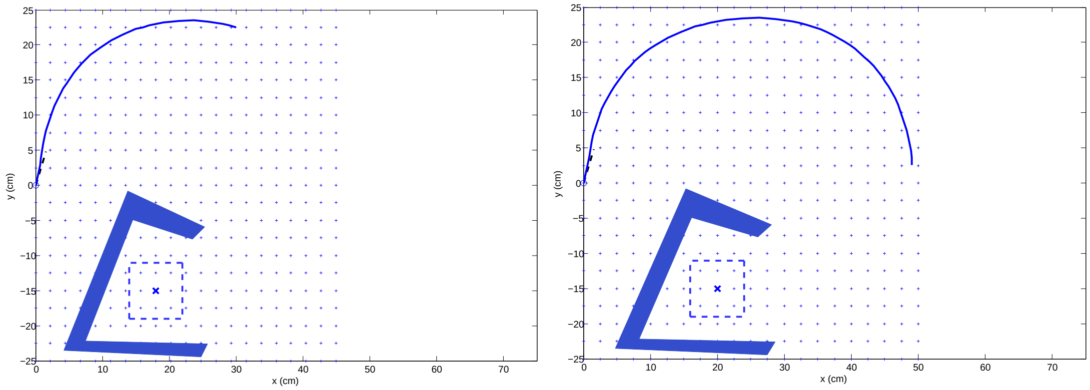

(c) t=44s

(d) t=72s

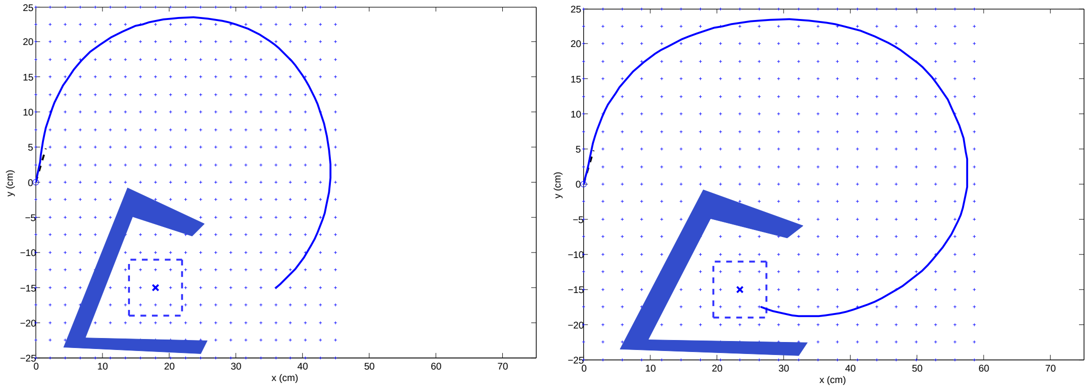

(e) t=92s

(f) t=112s. Target is reached.

Figure 4.11: Snapshots of the needle insertion in $\aleph_r$ with $q_{init} = [0\ 0\ 0]^T$. Tissue is denoted as blue crosses, target area with a dashed square. We have shown the entry point of the needle with a blue dot and the initial angle with a black, dashed line segment. Needle reaches its target in $112s$.

Chapter 5

Conclusion & Future Work

5.1 Conclusion

In this thesis, we presented a kinematic model for a bevel-tip flexible needle insertion within a tissue of state which can be captured by a time-dependent diffeomorphism. As general as this diffeomorphism can be, so as the developed needle model.

Based on this needle model, we presented a solution for a needle insertion into a planar tissue which is under a periodic motion. We modified a sampling-based planner to quickly explore the workspace of the needle to find a feasible path which will direct the needle to a goal position and avoid the obstacles which follow the same periodic motion of the tissue.

5.2 Discussion

Throughout this thesis, when we talked about changing the bevel-orientation we were aware that the time of changing the orientation might affect insertion. This is only an issue if this time is not neglectable in terms of the frequency of the tissue motion. Note that if the time of changing the orientation is big in terms of that frequency, than one should wait for the needle to complete a full cycle to be at that specific state in which the decision of orientation change is made.

5.3 Future Work

In this work, we have manually generated the obstacles and formed the workspace. One alternative to this could be to randomly generate polygonal obstacles. In this way, one can generate many workspaces and by testing the planner with these workspaces, a success rate can be acquired.

Also, when we generated the RRT we have kept the time between the nodes fixed. This time can be considered as a parameter and in future work this might help finding the optimal path by generating a set of trees with different time steps in-between the nodes.

Another thing to note is that, as we have mentioned in the corresponding sections in Chapter 4, finding the optimal entry point when applying the planning is very important for finding a feasible path for as shown in the experiments, initial position and the angle of the needle may lead to a tree which is blocked by the obstacles before reaching the goal. Therefore, this is an important fact to be considered in the future work.

Finally, in this work we have considered that the tissue, as it can be in a movement, remains undeformed with respect to the needle. To improve reality the model could be developed such that the insertion is done with a soft tissue which can be in any state defined by a time-dependent diffeomorphism. And from that step, the direction for this work could be to develop a mechanical model instead of a kinematic one.

Bibliography

[1] R. Alterovitz, M. S. Branicky, and K. Y. Goldberg. Constant-curvature motion planning under uncertainty with applications in image-guided medical needle steering. In *WAFR'06*, pages 319–334, 2006.

[2] R. Alterovitz, K. Y. Goldberg, and A. M. Okamura. Planning for steerable bevel-tip needle insertion through 2d soft tissue with obstacles. In *ICRA'05*, pages 1640–1645, 2005.

[3] N. Chentanez, R. Alterovitz, D. Ritchie, L. Cho, K. K. Hauser, K. Y. Goldberg, J. R. Shewchuk, and J. F. O'Brien. Interactive simulation of surgical needle insertion and steering. *ACM Trans. Graph.*, -:–, 2009.

[4] H. Choset, K. M. Lynch, S. Hutchinson, G. A. Kantor, W. Burgard, L. E. Kavraki, and S. Thrun. *Principles of Robot Motion: Theory, Algorithms, and Implementations*. MIT Press, 2005.

[5] M. R. Cox, J. L. McCall, J. Toouli, R. T. Padbury, T. G. Wilson, D. A. Wattchow, and M. Langcake. Prospective randomized comparison of open versus laparoscopic appendectomy in men. *World Journal of Surgery*, 20:263–266, 1996.

[6] S. P. DiMaio and S. E. Salcudean. Needle insertion modeling and simulation. *IEEE Transactions on Robotics and Automation*, 19:864 – 875, 2003.

[7] S. P. Dimaio and S. E. Salcudean. Interactive simulation of needle insertion models. *IEEE Trans. Biomedical Engineering*, 52:1167–1179, 2005.

[8] V. Duindam, J. Xu, R. Alterovitz, S. Sastry, and K. Y. Goldberg. Three-dimensional motion planning algorithms for steerable needles using inverse kinematics. *I. J. Robotic Res.*, -:789–800, 2010.

[9] M. Ghodoussi, S. E. Butner, and Y. Wang. Robotic surgery - the transatlantic case. *In Proc ICRA '02*, 2:1882–1888, 2002.

[10] G. Guthart and J. K. S. Jr. The intuitive telesurgery system: Overview and application. In *ICRA'00*, pages 618–621, 2000.

[11] K. K. Hauser, R. Alterovitz, N. Chentanez, A. M. Okamura, and K. Y. Goldberg. Feedback control for steering needles through 3d deformable tissue using helical paths. In *Robotics: Science and Systems'09*, 2009.

[12] R. J. W. III, N. J. Cowan, G. S. Chirikjian, and A. M. Okamura. Nonholonomic modeling of needle steering. In *ISER'04*, pages 35–44, 2004.

[13] R. J. W. III, J. Memisevic, and A. M. Okamura. Design considerations for robotic needle steering. In *ICRA '05*, 2005.

[14] D. L. James and D. K. Pai. Artdefo, accurate real-time elastic deformations of soft tissues for surgery simulation. *IEEE Trans. Visual. Comput. Graphics*, 33:65–72, 1999.

[15] S. Y. Ko, B. L. Davies, and F. R. y Baena. Two-dimensional needle steering with a programmable bevel inspired by nature: Modeling preliminaries. In *International Conference on Intelligent Robots and Systems*, 2010.

[16] E. J. Lobaton, J. Zhang, S. Patil, and R. Alterovitz. Planning curvature-constrained paths to multiple goals using circle sampling. In *ICRA'11*, pages 1463–1469, 2011.

[17] M. Marzouk, M. Khater, M. Elsadek, and A. Abdelmoghny. Laparoscopic versus open appendectomy. *Surgical Endoscopy*, 17:721–724, 2003.

[18] M. Michael J. Mack. Minimally invasive and robotic surgery. *the journal of the American Medical Association*, 285:–, 2001.

[19] S. Misra, K. T. Ramesh, and A. M. Okamura. Modelling of non-linear elastic tissues for surgical simulation. *Computer Methods in Biomechanics and Biomedical Engineering*, 13:811–818, 2010.

[20] T. U. Mnchen, T. J. Ortmaier, and T. J. Ortmaier. Motion compensation in minimally invasive robotic surgery, 2003.

[21] A. Nealen, M. Mller, R. Keiser, E. Boxerman, and M. Carlson. Physically based deformable models in computer graphics. *Computer Graphics Forum*, 25:809–836, 2005.

[22] S. Patil and R. Alterovitz. Interactive motion planning for steerable needles in 3d environments with obstacles. *Proc IEEE RAS EMBS Int Conf Biomed Robot Biomechatron*, -:893–899, 2010.

[23] S. Patil, J. van den Berg, and R. Alterovitz. Motion planning under uncertainty in highly deformable environments. In *Robotics: Science and Systems'11*, 2011.

[24] G. Picinbono, H. Delingette, and N. Ayache. Non-linear anisotropic elasticity for real-time surgery simulation. *Graphical Models*, 65:305–321, 2003.

[25] K. B. Reed, A. M. Okamura, and N. J. Cowan. Modeling and control of needles with torsional friction. *IEEE Transactions on Biomedical Engineering*, 56:–, 2009.

[26] T. R. Wedlick and A. M. Okamura. Characterization of pre-curved needles for steering in tissue. *Proc IEEE Eng Med Biol Soc.*, 2009:1200–1203, 2009.

[27] J. Xu, V. Duindam, R. Alterovitz, and K. Goldberg. Motion planning for steerable needles in 3d environments with obstacles using rapidly exploring random trees and backchaining. In *Proceedings of the IEEE Conference on Automation Science and Engineering*, pages 41–46, 2008.

[28] O. C. Zienkiewicz and R. L. Taylor. *Finite Element Method (5th Edition) Volume 1 - The Basis*. Elsevier, 2000.